

**Modeling rock damage during the long-term production process for hot dry rocks  
Effects of additional conductivity on the production performance and economic efficiency**

Xu, Fuqiang; Shi, Yu; Song, Xianzhi; Song, Guofeng; Li, Shuang

**DOI**

[10.1016/j.jclepro.2023.140298](https://doi.org/10.1016/j.jclepro.2023.140298)

**Publication date**

2023

**Document Version**

Final published version

**Published in**

Journal of Cleaner Production

**Citation (APA)**

Xu, F., Shi, Y., Song, X., Song, G., & Li, S. (2023). Modeling rock damage during the long-term production process for hot dry rocks: Effects of additional conductivity on the production performance and economic efficiency. *Journal of Cleaner Production*, 434, Article 140298. <https://doi.org/10.1016/j.jclepro.2023.140298>

**Important note**

To cite this publication, please use the final published version (if applicable).  
Please check the document version above.

**Copyright**

Other than for strictly personal use, it is not permitted to download, forward or distribute the text or part of it, without the consent of the author(s) and/or copyright holder(s), unless the work is under an open content license such as Creative Commons.

**Takedown policy**

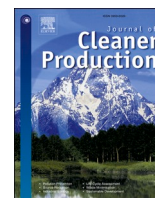
Please contact us and provide details if you believe this document breaches copyrights.  
We will remove access to the work immediately and investigate your claim.

***Green Open Access added to TU Delft Institutional Repository***

***'You share, we take care!' - Taverne project***

**<https://www.openaccess.nl/en/you-share-we-take-care>**

Otherwise as indicated in the copyright section: the publisher is the copyright holder of this work and the author uses the Dutch legislation to make this work public.



# Modeling rock damage during the long-term production process for hot dry rocks: Effects of additional conductivity on the production performance and economic efficiency

Fuqiang Xu<sup>a</sup>, Yu Shi<sup>b,\*</sup>, Xianzhi Song<sup>a</sup>, Guofeng Song<sup>c</sup>, Shuang Li<sup>a</sup>

<sup>a</sup> College of Petroleum Engineering, China University of Petroleum (Beijing), Beijing, China

<sup>b</sup> Faculty of Geosciences and Environmental Engineering, Southwest Jiaotong University, Chengdu, China

<sup>c</sup> Department of Geoscience and Engineering, Delft University of Technology, Delft, the Netherlands

## ARTICLE INFO

Handling Editor: Dr. Govindan Kannan

### Keywords:

Hot dry rocks  
Long-term production  
Rock damage  
Additional conductivity  
Production performance  
Economic efficiency

## ABSTRACT

Hot dry rocks (HDRs), as an essential renewable energy source, its development has received widespread attention, especially for heat extraction. The fracture is the main seepage and heat transfer channel of circulating fluid in dense HDR reservoirs, and its conductivity evolution significantly affects the production performance. Most existing studies have focused on the change of fracture conductivity under elastic deformation without considering the additional conductivity induced by rock damage. However, the additional conductivity may have significant implications for rational design and timely adjustment of the production scheme. Therefore, a three-dimensional model at the field-scale is established, and it is used to analyze the effect of additional conductivity on production performance and economic efficiency. To simplify the calculation, the actual forms of damage are equivalent to the macroscopic physical evolution of the matrix. Results show that the rock is mainly tensile failure affected by thermal stress during production. The occurrence of damage will increase the reservoir permeability and porosity, reduce Young's modulus, and then reduce the differential pressure and production temperature, with a maximum reduction of 2.21 MPa and 14.21 °C in the control case, respectively. The effects of injection temperature, Young's modulus, and injection mass flow on the production performance are significant, followed by Poisson's ratio. In contrast, production pressure and fracture initial permeability had less influence. The maximum differential economic benefit of the control case is up to 2.289 million RMB. This research proves the necessity of damage study during the long-term production of HDRs.

## 1. Introduction

As one of the alternative energy sources to fossil energy, the development and utilization of geothermal energy has received extensive attention worldwide (Song et al., 2018). Hot dry rocks (HDRs) geothermal has the characteristics of deep burial, high temperature, expansive reserves, dense lithology, etc (Wang et al., 2023). Enhanced geothermal system (EGS) is the primary way to develop HDR reservoirs (Tarkowski and Uliasz-Misiak, 2019), and relevant demonstration projects have been or are being built in the United States, France, China, Australia, etc. (Zhong et al., 2022; Xu et al., 2022). The method involves creating artificial fractures through manual processes in high-temperature, low-permeability reservoirs. These artificial and pre-existing natural fractures collectively form a complex fracture

network, establishing connectivity between injection and production wells. Subsequently, a working fluid is circulated to extract heat for practical applications (Xu et al., 2021).

In EGS, fractures are the main flow and heat transfer channels for circulating working fluids (Hofmann et al., 2016; Sun et al., 2020). In the long-term production, the rock matrix will undergo elastic deformation under continuous cooling due to cold fluid injection (Yang et al., 2023). Microcracks will even be induced near the fracture due to the weak degree of interparticle cementation, resulting in crack propagation and particle peeling (Xu et al., 2023a; Zhu et al., 2023).

Fracture conductivity is one of the essential attributes, which refers to the ability of fractures to allow fluid to pass under the action of reservoir in-situ stress. It has a significant impact on the production performance of HDR reservoirs (Ijeje et al., 2019; Li et al., 2020). For

\* Corresponding author.

E-mail address: [shiyu@swjtu.edu.cn](mailto:shiyu@swjtu.edu.cn) (Y. Shi).

<https://doi.org/10.1016/j.jclepro.2023.140298>

Received 6 August 2023; Received in revised form 24 October 2023; Accepted 18 December 2023

Available online 22 December 2023

0959-6526/© 2023 Elsevier Ltd. All rights reserved.

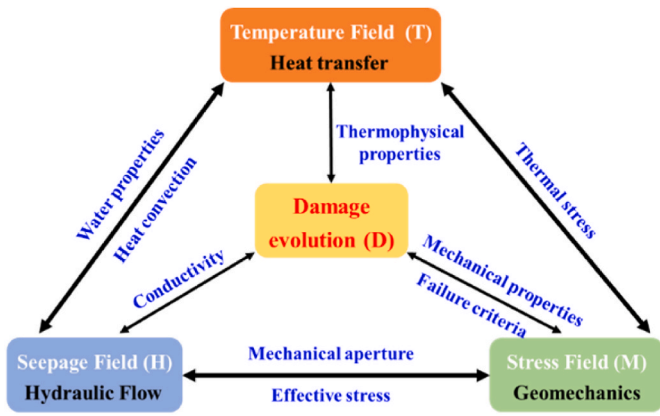


Fig. 1. Thermo-hydro-mechanical and damage (THM-D) coupling mechanism.

example, Shu et al. (2020) analyzed the effect of confining pressure and temperature on fracture hydraulics, concluding that the change in hydraulics has an essential impact on heat transfer properties. Guo et al. (2022) established the equations for the evolution of the permeability in major fractures, branch fractures, and natural fractures, and proved that the effect of fracture permeability evolution on thermal exploitation is necessary. Zhong et al. (2023) discovered that at high temperatures, mechanical deformation and chemical reactions on the fracture surfaces result in a reversal of hydraulic properties as the confining pressure increases. Song et al. (2024) established a fully coupled thermo-hydro-mechanical-chemical model to describe geothermal production. They quantified the contributions of mechanical and chemical factors, as well as their coupling relations, to the variations in fracture aperture during thermal extraction using a proposed calculation method of multi-physics magnitudes. Usually, fracture conductivity is generally expressed by the product of fracture permeability and aperture (Li et al., 2020), and the former can be characterized by the cubic law using the aperture (Wang et al., 2022). The change of fracture aperture caused by the matrix elastic deformation can be described by the normal displacement of the fracture surface (Song et al., 2022).

As previously mentioned, thermal stress and injection pressure jointly promote rock damage (Zhang et al., 2023), while the additional aperture change caused by damage is challenging to characterize

effectively (Xu et al., 2023a). In most current research, the damage is described as the physical property change of the rock matrix, which reduces the solving difficulty and improves the calculation speed. For example, Zhu's team (Zhu et al., 2014; Wei et al., 2015) used the maximum tensile stress criterion or the Mohr-Coulomb criterion to discriminate the damage in tension or shear mode of rock. They correlated the damage with the physical properties of the rock matrix, covering the feasibility of the above method. Li et al. (2017) studied shale gas production and fracturing using a number model, finding that the elastic modulus of the rock matrix element is gradually degraded as damage progresses. Guo et al. (2020) considered the damage caused by thermal stress during hydraulic fracturing, and they characterized the change of physical properties due to damage, such as elastic modulus, permeability, and thermal conductivity. Liu et al. (2020) presented a novel dual-damage thermal-mechanical model that accounts for the interplay among thermal conductivity, thermally-induced deformation, mechanical deformation, and damage to characterize the evolution of rock's thermal and mechanical properties during thermal treatment.

Most of the above studies are the damage evolution in rock fracturing or thermal treatment, and the duration is short, usually in hours, minutes, or even seconds (Guo et al., 2020; Zhang et al., 2022). There are currently known damage studies on tight oil reservoir development (Cheng et al., 2023) and hydrocarbon resource extraction (Lei et al., 2021), most of which are two-dimensional models. Still, few damage studies exist in producing an EGS for HDR reservoirs using the 3D model. To analyze the effects of additional conductivity caused by damage, the current research is organized as follows: In Section 2, considering the thermo-hydro-mechanical-damage (THM-D) coupling, a numerical model of the injection-production system of multiple vertical wells is established; Section 3 analyzes the numerous physics evolution characteristics, and compares the performance under various parameters with and without damage; In Section 4, combining electricity costs and heat sales revenues, it discusses the effects of damage on economic benefits; Finally, Section 5 summarizes the main conclusions.

## 2. Methodology

### 2.1. Model assumptions

For the convenience of research and analysis, the EGS mentioned is considered idealized: the outer side of the reservoir is surrounded by

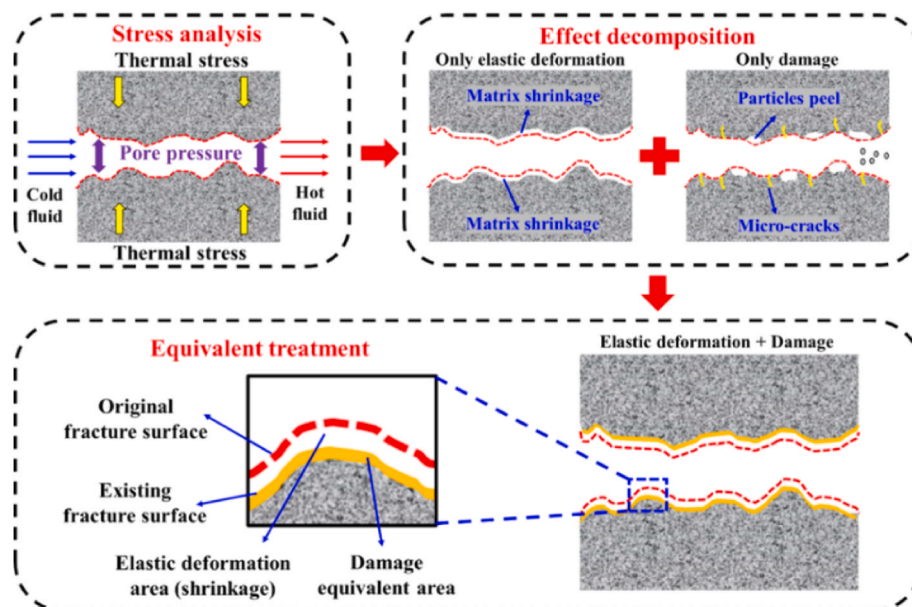


Fig. 2. Elastic deformation and damage analysis at fracture surfaces.

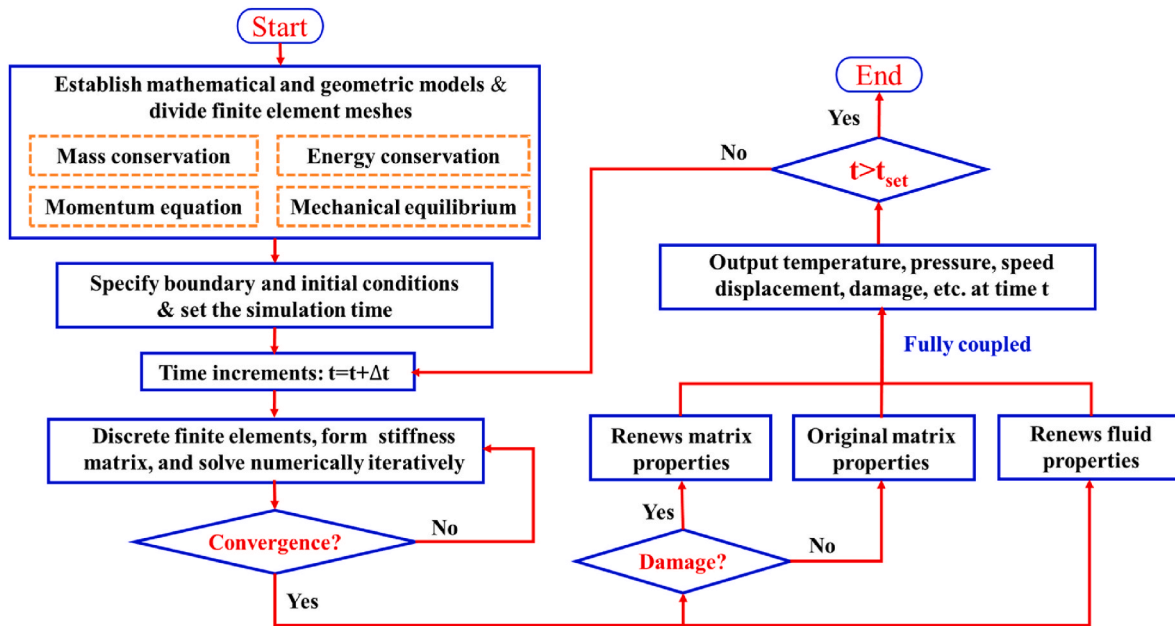


Fig. 3. Finite element solution idea.

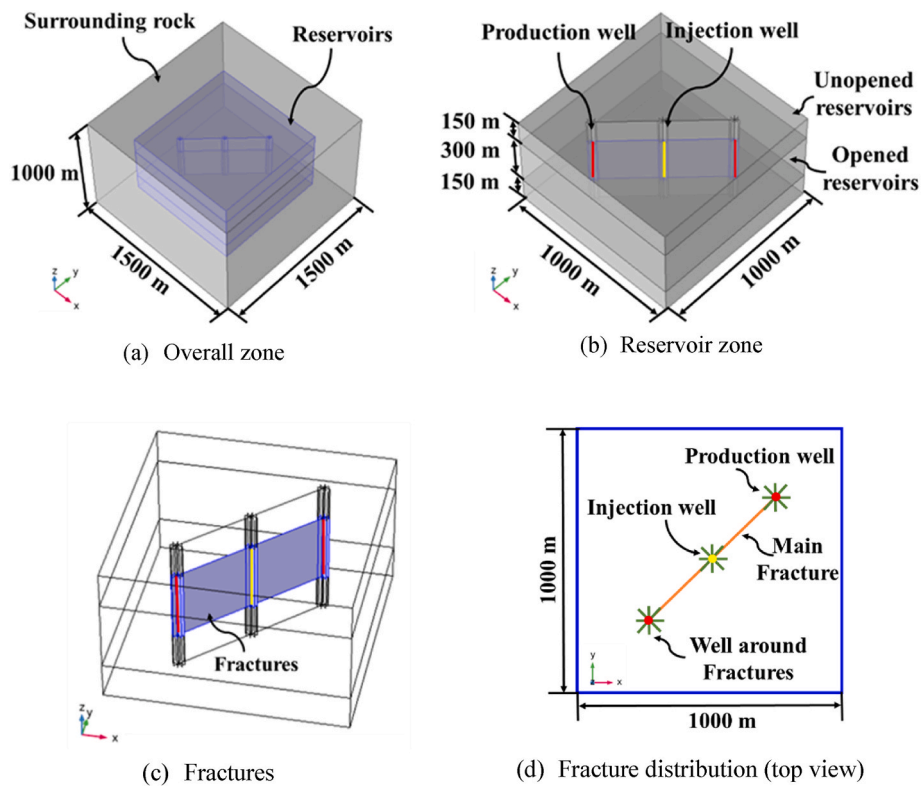


Fig. 4. Computational zone for the numerical model.

surrounding rock, and the reservoir is considered as the stimulated volume that contains activated natural fractures and induced minor fractures by stimulation (Song et al., 2018). There are multiple artificial fractures in the reservoir, representing primary fractures generated by hydraulic fracturing (Xu et al., 2021). The fracture permeability is much higher than the reservoir's, so the fracture is distinguished from the reservoir (Song et al., 2018).

The basic assumptions are made as follows: (1) reservoirs and surrounding rock are simplified as the equivalent continuous porous

medium with homogeneous and isotropic properties (Wang et al., 2020a; Song et al., 2022), but the exception is Young's modulus and Poisson's ratio, which will be given below; (2) under simulated conditions, the water does not evaporate and is considered liquid, does not react with rocks, and single-phase fluid flows in reservoirs and fractures meet Darcy's Law (Chen et al., 2019); (3) heat transfer in fractured fluids and matrix uses local non-thermal equilibrium assumptions, and the convective heat transfer coefficient is constant (Zhang et al., 2018); (4) the permeability of the surrounding rock is much smaller than that of

**Table 1**  
Physical properties of the surrounding rock, reservoir, and fractures (Lei et al., 2020, 2021; Zhang et al., 2021).

Items	Surrounding rock	Reservoir	Fracture
Density, kg/m <sup>3</sup>	2800	2600	1200
Thermal conductivity, W/(m·°C)	3.0	2.9	2.0
Isobaric heat capacity, J/(kg·°C)	1000	950	800
Porosity	0.01	0.03	0.60
Initial permeability, m <sup>2</sup>	10 <sup>-18</sup>	3.5 × 10 <sup>-16</sup>	3.5 × 10 <sup>-11</sup>
Thermal expansion coefficient, 1/°C	5 × 10 <sup>-6</sup>	5 × 10 <sup>-6</sup>	5 × 10 <sup>-6</sup>
Average Young's modulus, GPa	50	50	50
Tensile strength, MPa	10.5	10.5	10.5
Initial compressive strength, MPa	350	350	350
Average Poisson's ratio	0.25	0.25	0.25
Biot-Willis coefficient	0.7	0.7	0.7
Normal stiffness, GPa/m	/	/	80
Shear stiffness, GPa/m	/	/	50

**Table 2**  
Parameters of the initial conditions (Lei et al., 2020, 2021; Zhang et al., 2022).

Items	Value
Pressure at 3000 m, MPa	40
Pressure gradient, Pa/m	5000
Temperature at 3000 m, °C	250
Temperature gradient, °C/m	0.05
Injection rate, kg/s	50
Injection temperature, °C	50
Initial real fracture aperture, m	3.8 × 10 <sup>-4</sup>
ψ coefficient	0.5
Convective heat transfer coefficient, W/(m <sup>2</sup> ·°C)	3000
Internal friction angle, °	30

reservoirs and fractures (Xu et al., 2023a); (5) ignore water loss in the matrix during damage evolution.

The physical properties of water vary with the temperature (Holzbecher, 1998).

$$\mu_w = \begin{cases} 10^{-3} \times (1 + 0.015512 \times (T - 20))^{-1.572}, & 0^\circ C \leq T \leq 100^\circ C \\ 0.2414 \times 10^{\left(\frac{247.8}{T+133.15}\right)} \times 10^{-4}, & 100^\circ C \leq T \leq 280^\circ C \end{cases} \quad (1)$$

where  $\mu_w$  (Pa·s) is the water dynamic viscosity;  $T$  (°C) is the temperature.

$$\rho_w = \begin{cases} 996.9 \times (1 - 3.17 \times 10^{-4} \times (T - 20) - 2.56 \times 10^{-6} \times (T - 20)^2), & 20^\circ C \leq T \leq 175^\circ C \\ 1758.4 + 1000 \times \left( \begin{aligned} &-0.00484(T+273.15) + 1.01 \times 10^{-5}(T+273.15)^2 \\ &-9.85 \times 10^{-9} \times (T+191.9)(T+273.15)^2 \end{aligned} \right) & 175^\circ C \leq T \leq 280^\circ C \end{cases} \quad (2)$$

where  $\rho_w$  (kg/m<sup>3</sup>) is the water density, kg/m<sup>3</sup>.

$$\begin{cases} c_w = 12010.1 - 80.4(T + 273.15) + 0.3(T + 273.15)^2 - 5.4 \times 10^{-4}(T + 273.15)^3 + 3.6 \times 10^{-7}(T + 273.15)^4, & 20^\circ C \leq T \leq 280^\circ C \\ \lambda_w = -0.8691 + 0.0089(T + 273.15) - 1.5837 \times 10^{-5}(T + 273.15)^2 + 7.9754 \times 10^{-9}(T + 273.15)^3, & 20^\circ C \leq T \leq 280^\circ C \end{cases} \quad (3)$$

where  $c_w$  (J/(kg·°C)) is the water heat capacity at constant pressure;  $\lambda_w$  (W/(m·°C)) is the water's thermal conductivity.

## 2.2. Governing equations

Fig. 1 depicts the thermo-hydro-mechanical and damage (THM-D) coupling mechanism. The interplay between fluid flow, heat transfer, and stress evolution is achieved through real-time transmission of multiple variables, including pressure, velocity, temperature, damage factors, fracture aperture, etc. Notably, damage evolution serves as a pivotal link. Specifically, the occurrence of damage alters the thermo-physical properties of rocks, with thermal stress stemming from temperature field evolution being a significant contributor to rock damage; stress serves as the foundation for judging rock damage, and damage occurrence impacts the mechanical properties of the rock; damage influences conductivity and consequently the seepage field, which, in turn, can influence damage by affecting the temperature and stress fields (Xu et al., 2023a; Song et al., 2022).

Model solutions include the mass conservation equation and seepage equation, heat transfer equation, and equilibrium equation of rock deformation. Considering the apparent difference in the physical properties of fractures and matrix, it establishes separate corresponding equations, and there is mass and energy exchange between them.

### 2.2.1. Fluid flow

The seepage equation is described by Darcy's law (Chen et al., 2019), and the corresponding equations in the rock matrix and fractures are as follows (Shi et al., 2019a):

$$\vec{u} = -\frac{k_m}{\mu_f} (\nabla p + \rho_f g \nabla z) \quad (4)$$

$$\rho_f S_m \frac{\partial p}{\partial t} + \nabla \cdot (\rho_f \vec{u}) = -\rho_f \alpha_B \frac{\partial e}{\partial t} - Q_f \quad (5)$$

$$\vec{u}_f = -\frac{k_f}{\mu_f} (\nabla_T p + \rho_f g \nabla_T z) \quad (6)$$

$$d_f \rho_f S_f \frac{\partial p}{\partial t} + \nabla_T \cdot (d_f \rho_f \vec{u}_f) = -d_f \rho_f \alpha_B \frac{\partial e}{\partial t} + d_f Q_f \quad (7)$$

where  $\vec{u}$  (m/s) and  $\vec{u}_f$  (m/s) are the flow velocity in the matrix and fractures, respectively;  $k_m$  (m<sup>2</sup>) and  $k_f$  (m<sup>2</sup>) are the permeability of the rock matrix and fractures separately;  $\mu_f$  (Pa·s) is the fluid viscosity;  $p$  (Pa) is the pressure;  $\rho_f$  (kg/m<sup>3</sup>) is the fluid density;  $g$  (m/s<sup>2</sup>) is the gravity acceleration;  $t$  (s) is the time;  $e$  is the volumetric strain caused by rock deformation, and its expressions will be given below;  $Q_f$  (kg/(m<sup>3</sup>·s)) is the mass transfer between the rock matrix and fractures;  $d_f$  (m) is the fracture aperture.

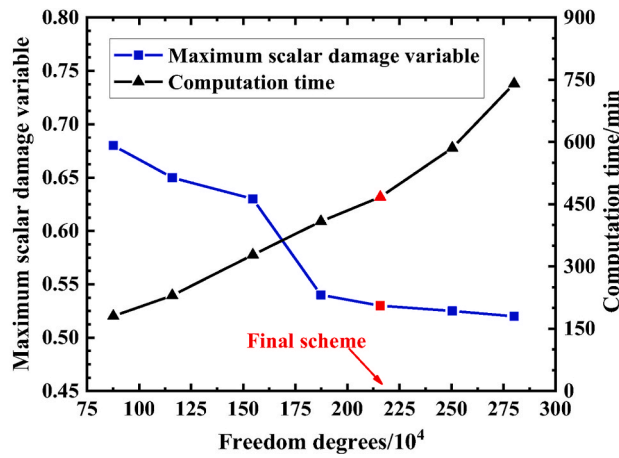
$S$  (Pa<sup>-1</sup>) is the storage coefficient that considers the fluid and rock compressibility, as follows:

$$S = \varphi C_f + (\alpha_B - \varphi) \frac{(1 - \alpha_B)}{K_d} \quad (8)$$

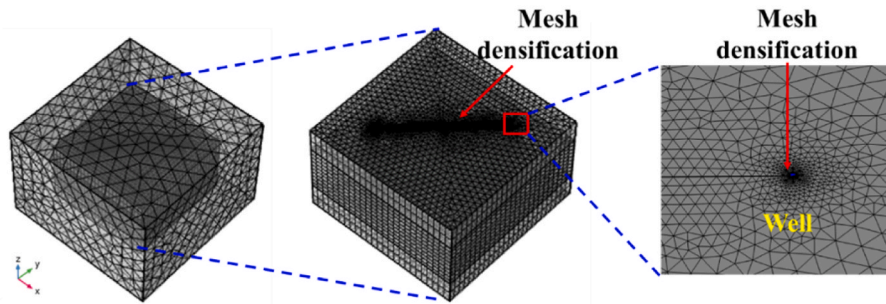
$\alpha_B$  is the Biot-Willis coefficient (Biot, 1962), as follows:

$$\alpha_B = 1 - \frac{K_d}{K_s} \quad (9)$$

where  $\varphi$  is the porosity;  $C_f$  (Pa<sup>-1</sup>) is the fluid compressibility;  $K_d$  (Pa) is



(a) Mesh independence analysis



(b) Mesh partitioning scheme

Fig. 5. Meshing scheme for the computational zone.

the drained bulk modulus of the porous matrix of the same material;  $K_s$  (Pa) is the bulk modulus of a homogeneous block of the solid material.

Affected by elastic deformation, the fracture permeability changes, which is mainly caused by the deformation along the normal direction of the fracture surface, and the expression is as follows (Witherspoon et al., 1979):

$$k_f = \frac{d_h^2}{12} = \frac{(d_{h0} + \psi \Delta d_{f,n})^2}{12} \quad (10)$$

where  $d_h$  (m) is the hydraulic aperture;  $d_{h0}$  (m) represents the initial hydraulic aperture;  $\psi$  is the coefficient describing the transformation of hydraulic aperture and geometric aperture with a range generally from 0.5 to 1;  $\Delta d_{f,n}$  is the normal deformation value of the geometric aperture.

### 2.2.2. Heat transfer

Similarly, the heat transfer equations in the rock matrix and fractures are given separately, as follows (Wang et al., 2022):

$$(\rho c_p)_{eff,m} \frac{\partial T_m}{\partial t} + \rho_f c_{p,f} \nabla \cdot (\vec{u} \cdot T_m) - \nabla \cdot (\lambda_{eff,m} \nabla T_m) = -Q_{f,E} \quad (11)$$

$$d_f (\rho c_p)_{eff,f} \frac{\partial T_f}{\partial t} + d_f \rho_f c_{p,f} \nabla_T \cdot (\vec{u}_f \cdot T_f) - \nabla_T \cdot (d_f \lambda_{eff,f} \nabla T_f) = d_f Q_{f,E} \quad (12)$$

where  $(\rho c_p)_{eff}$  ( $J/(m^3 \cdot ^\circ C)$ ) and  $\lambda_{eff}$  ( $W/(m \cdot ^\circ C)$ ) are the effective volumetric capacity and the effective thermal conductivity, respectively, which are determined by:

$$(\rho c_p)_{eff} = (1 - \phi) \rho_s c_{p,s} + \phi \rho_f c_{p,f} \quad (13)$$

$$\lambda_{eff} = (1 - \phi) \lambda_s + \phi \lambda_f \quad (14)$$

where  $T_m$  ( $^\circ C$ ) is the rock matrix temperature;  $c_{p,f}$  ( $J/(kg \cdot ^\circ C)$ ) is the fluid

thermal capacity;  $T_f$  ( $^\circ C$ ) is the fracture temperature;  $\rho_s$  ( $kg/m^3$ ) is the solid density;  $c_{p,s}$  ( $J/(kg \cdot ^\circ C)$ ) is the solid thermal capacity;  $\lambda_s$  ( $W/(m \cdot ^\circ C)$ ) and  $\lambda_f$  ( $W/(m \cdot ^\circ C)$ ) are the solid and fluid thermal conductivity, respectively.

$Q_{f,E}$  ( $W/m^3$ ) is the heat transfer between the reservoir matrix and fractures, which can be given by the following equation (Taler, 2019):

$$q_{f,E} = h_f (T_f - T_m) \quad (15)$$

where  $h_f$  ( $W/(m^2 \cdot ^\circ C)$ ) is the convective heat transfer coefficients.

### 2.2.3. Mechanical deformation

According to the transient equation and considering that temperature changes induce thermal stresses within the rock, the rock deformation is described as follows (Shi et al., 2019b):

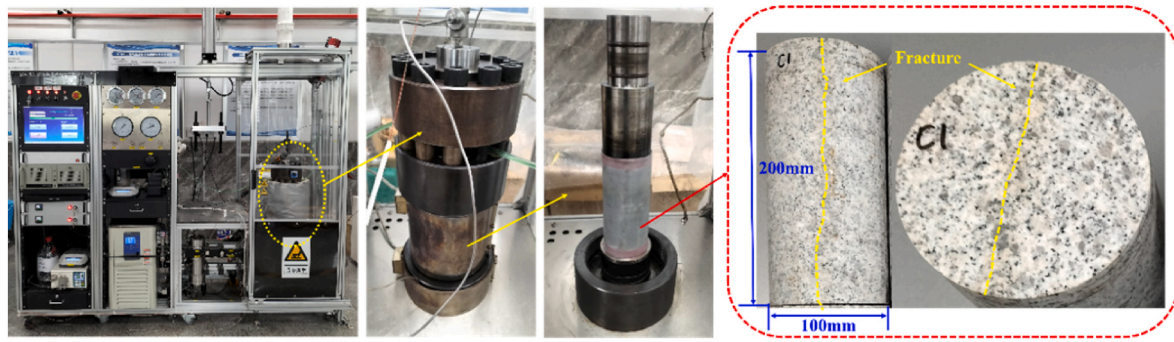
$$\frac{E}{2(1+\nu)} v_{i,ij} + \frac{E}{2(1+\nu)(1-2\nu)} v_{j,ji} - \alpha_B p \delta_{ij} - \frac{E}{1-2\nu} \alpha_T (T - T_0) + F_i = 0 \quad (16)$$

where  $E$  (Pa) is Young's modulus;  $\nu$  is the Poisson's ratio;  $v$  (m) is the displacement;  $\delta_{ij}$  is the Kroneck symbol;  $\alpha_T$  ( $1/^\circ C$ ) is the thermal expansion coefficient of rocks;  $T_0$  ( $^\circ C$ ) is the initial temperature;  $F_i$  is the body force per unit volume in the  $i$ -coordinate.

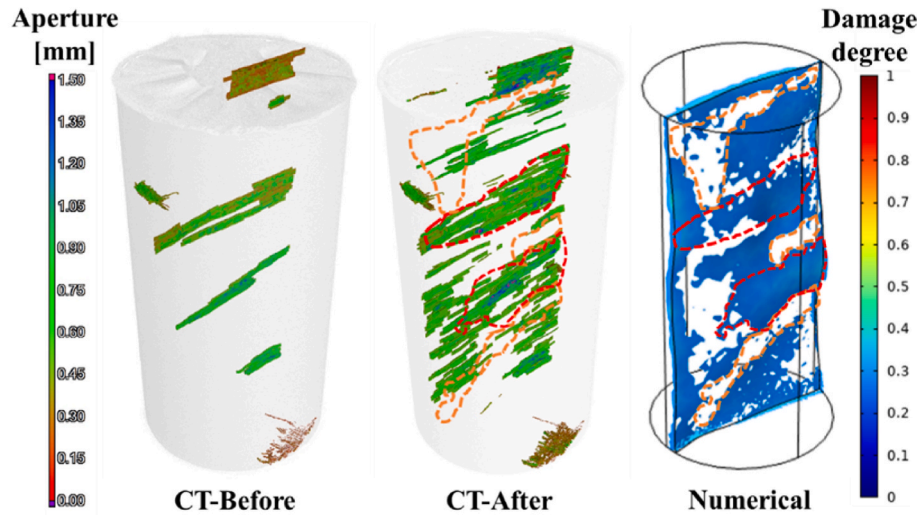
The correlation between the volumetric strain in Eq. (5), (7) is expressed by (Ju et al., 2011):

$$e = \frac{\sigma_e}{K_d} = \frac{(1-2\nu)}{E} (\sigma_1 + \sigma_2 + \sigma_3) \quad (17)$$

where  $\sigma_e$  (Pa) is effective stress;  $\sigma_1$  (Pa),  $\sigma_2$  (Pa), and  $\sigma_3$  (Pa) are the first, second, and third effective principal stresses, respectively, which are obtained by superimposing the principal stress and the pore pressure (Rutqvist et al., 2001). Moreover, the tensile stress is positive, and



(a) Experimental equipment and rock samples



(b) CT scan results and numerical results

Fig. 6. Comparison of numerical results and experimental results.

**Table 3**  
Study protocols for numerical simulation (Lei et al., 2020).

Experiment type	Parameters	Value Range
<b>Injection-mining parameters</b>	Injection temperature, °C	40, 50, 60, 70
	Injection mass flow, kg/s	30, 40, 50, 60
	Average production pressure, MPa	35.5, 37.5, 39.5, 41.5
<b>Reservoir physical properties</b>	Young's modulus, GPa	45.0, 47.5, 50.0, 52.5
	Poisson's ratio	0.175, 0.200, 0.225, 0.250
	Fracture initial permeability, $10^{-11} \text{ m}^2$	2.0, 3.5, 5.0, 6.5

compressive stress is negative in this model.

#### 2.2.4. Damage evolution

Maximum tensile stress criterion ( $F_t \geq 0$ ) or the More-Coulomb criterion ( $F_s \geq 0$ ) is used to determine whether the rocks are damaged (Zhu and Tang, 2004):

$$\begin{cases} F_t = \sigma_1 - f_t = 0 \\ F_s = -\sigma_3 + \sigma_1 \frac{1 + \sin \varphi_f}{1 - \sin \varphi_f} - f_c = 0 \end{cases} \quad (18)$$

where  $f_t$  (Pa) and  $f_c$  (Pa) are the tensile strength and compressive strength, respectively;  $\varphi_f$  (°) is the internal friction angle. In particular,

tensile damage is judged first, then shear damage is judged without tensile damage (Zhu et al., 2013).

Commonly used rock damage models in existing studies include the elastic-brittle damage model and the elastic softening damage model. Different from hydraulic fracturing in HDR reservoirs, the damage in the production is a gradual accumulation, so the elastic softening model is used to characterize the above damage evolution as follows (Zhu et al., 2013):

$$\omega = \begin{cases} 1 - |\varepsilon_{t0}/\varepsilon_1|^n, & F_t \geq 0, F_s < 0 \\ 0, & F_t < 0, F_s < 0 \\ 1 - |\varepsilon_{c0}/\varepsilon_3|^n, & F_t < 0, F_s \geq 0 \end{cases} \quad (19)$$

where  $\omega$  is a scalar damage variable, evolving from 0 for the intact material to 1 for the fully damaged material;  $\varepsilon_1$  and  $\varepsilon_3$  are the major principal strain and the minor principal strain respectively;  $\varepsilon_{t0}$  and  $\varepsilon_{c0}$  are the maximum tensile principal strain and the maximum compressive principal strain when tensile and shear damages occur, respectively,  $\varepsilon_{t0} = f_t/E$ ,  $\varepsilon_{c0} = -f_c/E$ ;  $n$  is a constitutive coefficient specified as 2.0 (Wei et al., 2015).

During the long-term mining process, the matrix near the fracture will undergo different forms and degrees of damage, including microcrack initiation, propagation, particle peeling, etc (Xu et al., 2023a). In numerical simulation, it is not easy to achieve efficient and accurate characterization of the above phenomena. Therefore, an equivalent

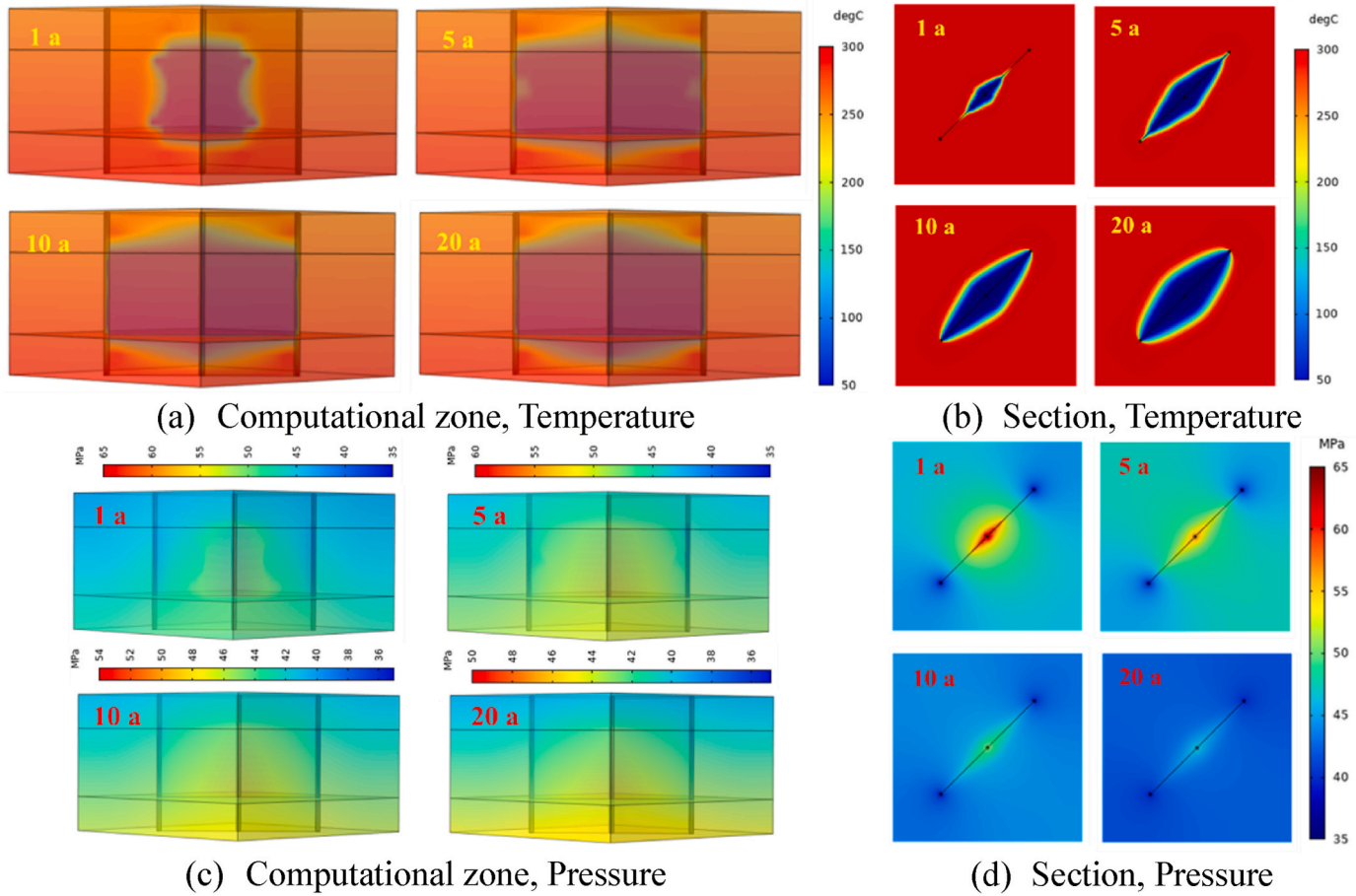


Fig. 7. Temperature and pressure field evolution.

method is adopted. In Fig. 2, the various forms of damage equal the damaged area (orange zone), which coexists with the matrix, distinct from the void regions (white zone) caused by matrix elastic deformation. The physical parameters of the damaged area are significantly different from the non-damaged area, including porosity, permeability, Young's modulus, mechanical strength, and thermal conductivity (Zhu and Tang, 2004; Zhu and Wei, 2011; Li, 2018).

After the rock is damaged, its Young's modulus and compressive strength decrease, and the porosity and permeability increase accordingly. The porosity has a linear relationship with the damage variable (Li, 2018), and the permeability has an exponential relationship with the damage variable (Zhu and Wei, 2011):

$$\begin{cases} E = (1 - \omega)E_0 \\ f_c = (1 - \omega)f_{c0} \end{cases} \quad (20)$$

$$\begin{cases} \varphi_m = \varphi_0 + (\varphi_f - \varphi_0)\omega \\ k_m = k_{m0} \left(\frac{\varphi_m}{\varphi_0}\right)^3 e^{\beta\omega} \end{cases} \quad (21)$$

$$\lambda_s(T, \omega) = \lambda_{s0} e^{\omega/\delta_T} \quad (22)$$

where  $E_0$  (Pa) is Young's modulus of the undamaged rock;  $f_c$  (Pa) and  $f_{c0}$  (Pa) are the compressive strength (Pa) of the damaged and undamaged element, respectively;  $\varphi_m$ ,  $\varphi_0$ , and  $\varphi_f$  are the matrix porosity, initial matrix porosity, and fracture porosity, respectively;  $k_{m0}$  ( $m^2$ ) is the initial permeability of the rock matrix, and  $\beta$  is damage-permeability effect coefficient to indicate the effect of damage on the permeability (Zhu and Wei, 2011; Lei et al., 2021);  $\lambda_s$  (W/( $m \cdot ^\circ C$ )) is the thermal conductivity;  $\delta_T$  is a coefficient, and it reflects the effect of damage on

thermal conductivity.

### 2.3. Model solution

Mass conservation, energy conservation, momentum equation, and mechanical equilibrium of the model are solved in the finite element solver. The primary variables solved include pore pressure, temperature, damage, and displacements along three directions, and the other variables are calculated based on primary variables. Considering the strong nonlinearity, a time-stepping approach employing the stable implicit backward differentiation formula (BDF) method is used. The solution idea is shown in Fig. 3. The total period is 20 years, and the time step is 1.0 d.

#### 2.3.1. Computational model

The model computational zone is shown in Fig. 4(a), a cuboid with the size of 1500 m  $\times$  1500 m  $\times$  1000 m, and its depth ranges from 3000 m to 4000 m, consisting of surrounding rock, reservoirs, and fractures. Moreover, the size of the cuboid reservoir is 1000 m  $\times$  1000 m  $\times$  600 m, located in the center of the computational zone. The reservoir is divided into three parts, the upper, middle, and lower sections, which are unopened, open, and unopened reservoirs, with a thickness of 150 m, 300 m, and 150 m, as shown in Fig. 4(b). Opened reservoir (stimulated reservoir volume, SRV) refers to the reservoir section of the wellbore through perforation and other processes, which can achieve fluid injection and production.

Two production wells are located on both sides of the injection well (well spacing 350 m), with a diameter of 0.10 m and a length of 300 m, i. e., the same thickness as the opened reservoir. Fracture is within the reservoir, including a primary fracture and fractures around the well, as

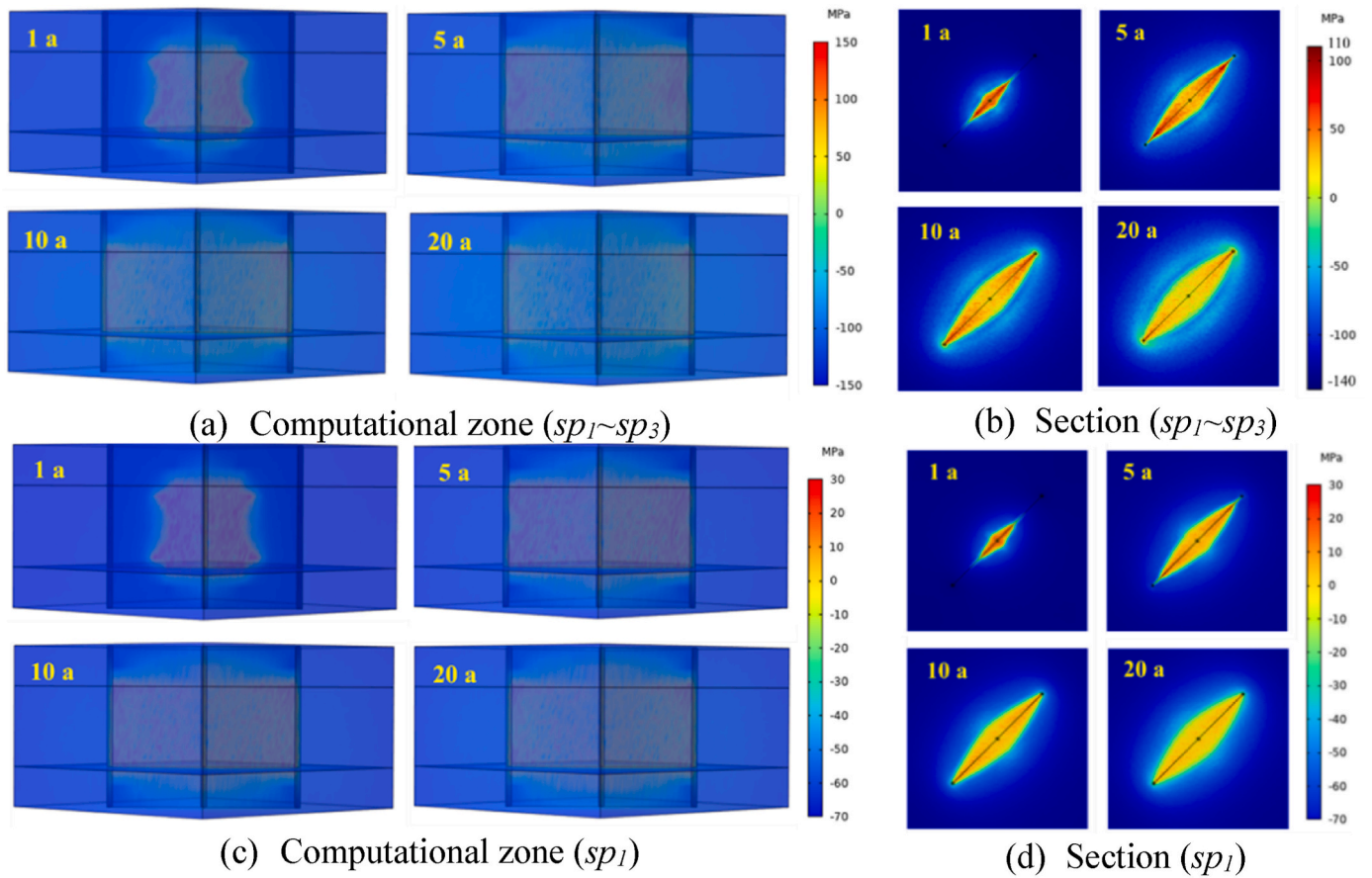


Fig. 8. Stress field evolution.

shown in Fig. 4(c)–(d). The large number of fractures around the well is the remarkable fracturing effect, and the half-length of each fracture is 10 m. Moreover, the primary fracture can be considered the superposition of the fracturing fracture and the original natural fracture. The physical properties of the surrounding rock, reservoir, and fractures utilized in the model are listed in Table 1 (Lei et al., 2020, 2021; Zhang et al., 2021).

It considers the heterogeneity effect of Young's modulus and Poisson's ratio on the results, so their expressions in Table 1 are the average value. The heterogeneity is defined as follows:

$$f_0(x, y, z) = f_m(x, y, z) \text{Rand} \quad (23)$$

where  $f_0(x, y, z)$  is the initial average value of Young's modulus or Poisson's ratio;  $\text{Rand}$  is the random number. After the above heterogeneous treatment, Young's modulus and Poisson's ratio range are from 42.2 GPa to 58.8 GPa and 0.23–0.27, respectively.

### 2.3.2. Initial and boundary conditions

The model uses flow inlet (injection well) and pressure outlet (production well), and the production pressure is 3 MPa less than the initial pressure of the reservoir to ensure that fluid is not generally flashed (Yu et al., 2022). All model boundaries are set to no-flow and open temperature boundaries (Shi et al., 2019a), i.e., continuous heat replenishment around the reservoir. Other initial and boundary conditions of the model are shown in Table 2 (Lei et al., 2020, 2021; Zhang et al., 2022). Most of the injection parameters and reservoir properties are selected based on the data from the Qiabuqia geothermal field of Northwest China. At the initial moment, the rock matrix is in a state of compressive stress under the influence of in-situ stress. In the control case, the magnitude of the compressive stress on three axes is 68 MPa.

### 2.3.3. Finite element discretization

Triangular elements are generated on the top surface of the reservoir, and mesh densification is performed around injection wells, production wells, and fractures. Then, the meshes are swept vertically to the bottom surface of the reservoir to produce triangular prismatic elements. The surrounding rock zone meshes using a free tetrahedron. The meshing scheme for the computational zone is shown in Fig. 5.

The number of meshes will influence the result. After mesh independence analysis, a scheme with a mesh number of 124,000 and the corresponding number of freedom degrees of 2.16 million is selected, which ensures high solution speed and calculation accuracy.

### 2.4. Model validation

In this paper, the THM-D coupling model is established. Moreover, seepage and heat transfer processes in the fractures are considered. The T-H-M coupling model and fracture seepage-heat transfer model have been extensively demonstrated in previous studies (Song et al., 2018; Shi et al., 2023; Xu et al., 2023a). Therefore, this paper focuses on verifying the accuracy of damage evolution.

Fig. 6(a) displays the experimental setup and rock samples used for verification, with single fractures penetrating the rock samples. Detailed physical properties of the rocks can be found in the available literature (Xu et al., 2023a). Before and after cold water injection, CT scans are performed. The experimental conditions included a temperature of 280 °C, an injection volume flow rate of 4.0 ml/min, an axial pressure of 20 MPa, and a confining pressure of 10 MPa. The duration of the experiment is set at 20 min. After the second CT scan, the fracture morphology is captured and incorporated into the numerical model through topography scanning, followed by simulation under identical conditions.

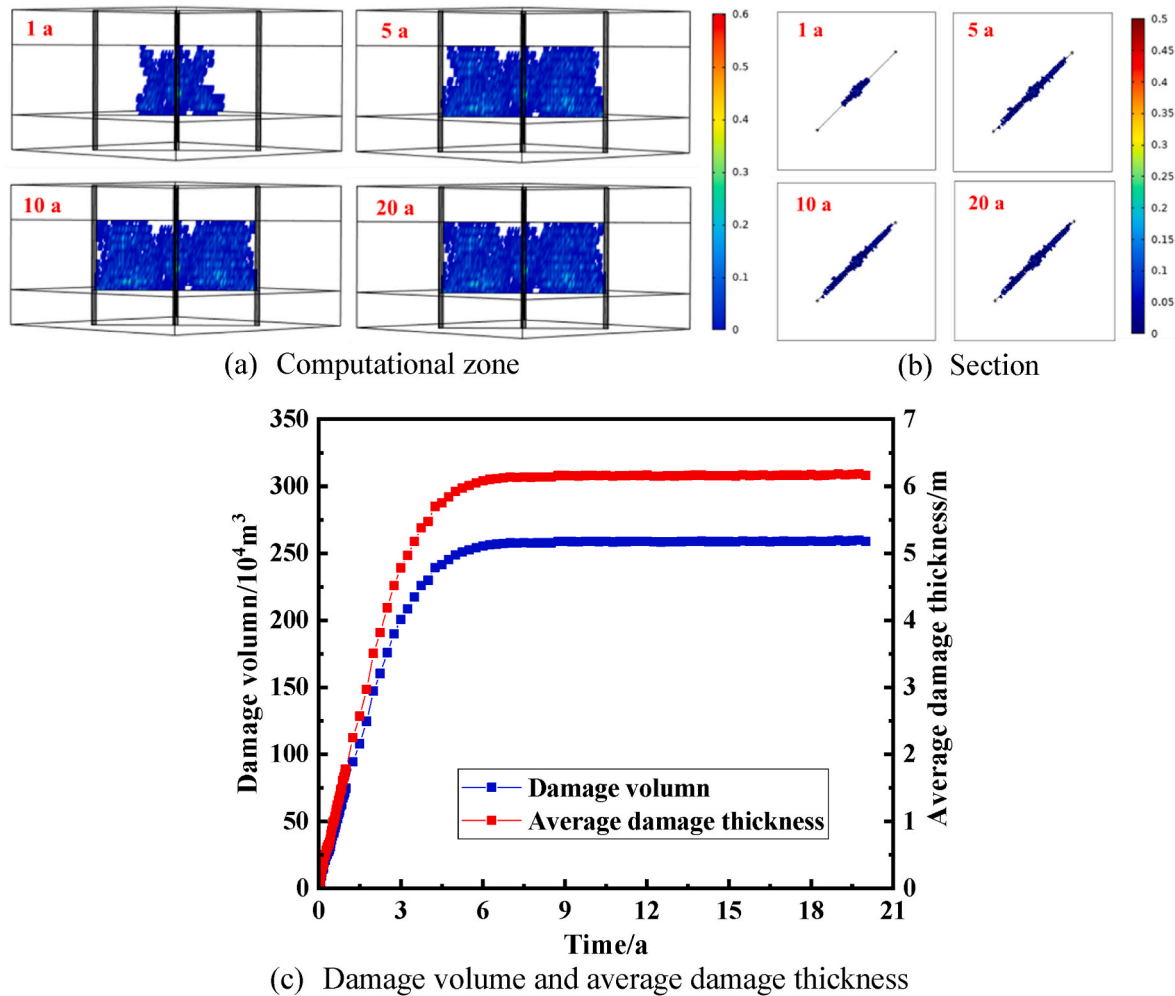


Fig. 9. Damage evolution.

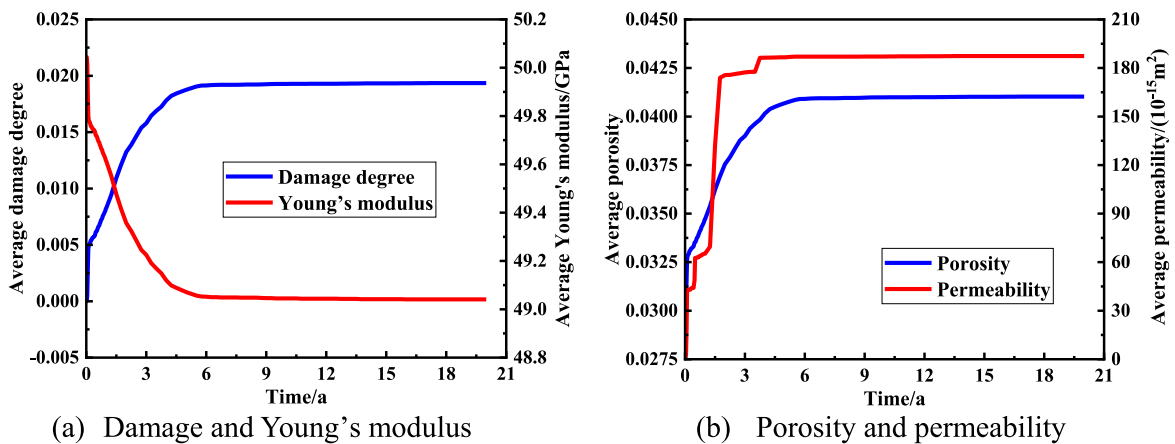


Fig. 10. Damage and average physical property changes.

As depicted in Fig. 6(b), the evolution of damage and variations in fracture aperture primarily occur near the fracture. The fracture aperture exhibits more noticeable changes in areas with greater damage degrees. In comparing numerical and experimental results, a good correlation is observed between the damaged predominant regions (red) and undamaged areas (orange) at the fracture. Overall, the experimental and numerical results align with the requirements, confirming the capability to simulate the damage evolution process effectively.

### 3. Analysis of numerical results

#### 3.1. Evaluation indicators and study protocols

Three evaluation indicators are defined to analyze the comparison results, i.e., weighted damage volume, differential pressure, and production temperature.

Damage characteristics include the damage volume and degree

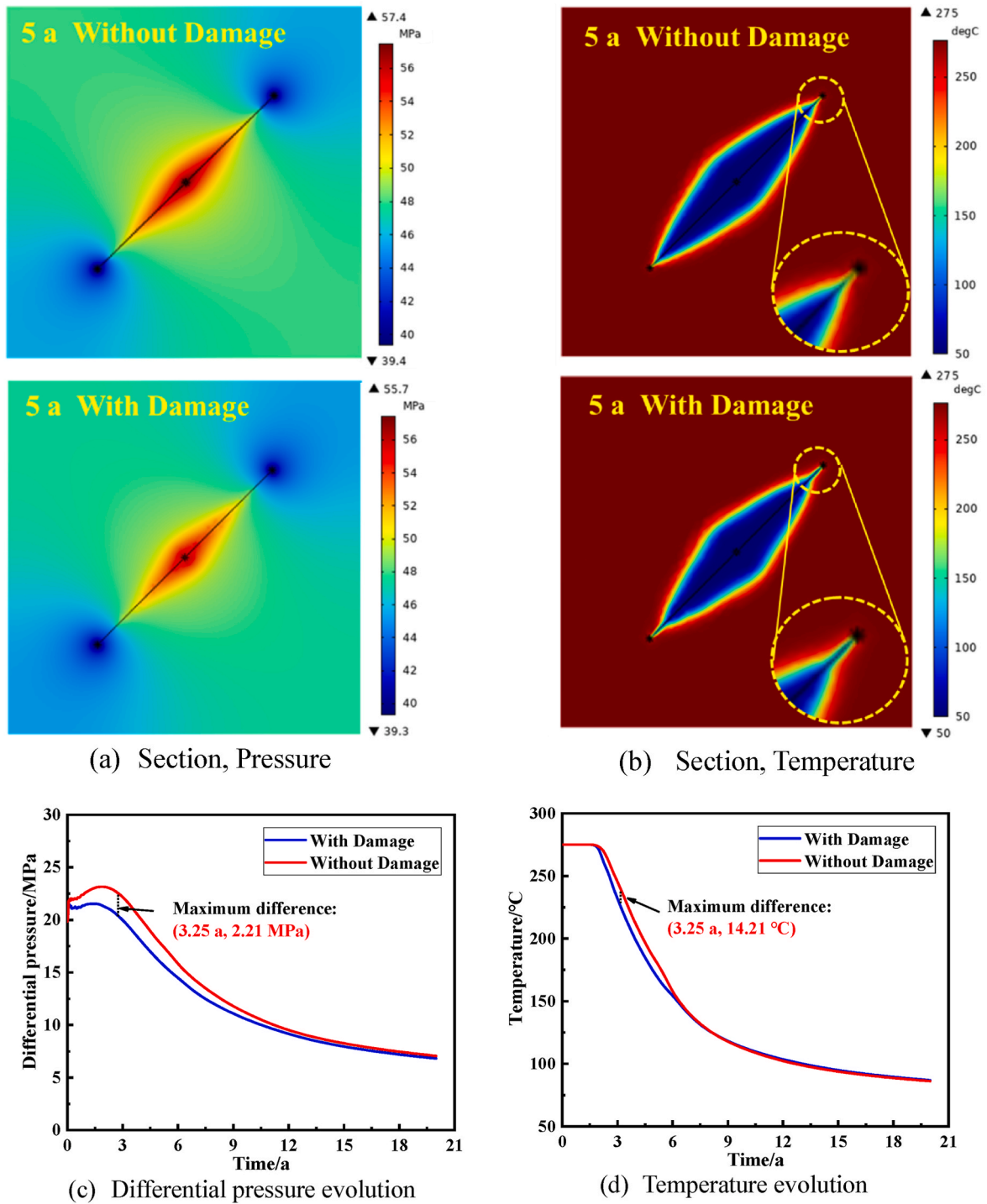


Fig. 11. Differential pressure and temperature comparison.

evolution, and it defines the “weighted damage volume”:

$$\chi = \sum_{j=0}^1 \frac{j + (j + 0.1)}{2} V_{\text{damage},j \sim (j+0.1)}(t) \times 100\%, \quad j = 0, 0.1, \dots, 1.0 \quad (24)$$

In the above equation, the 0–1 damage is divided into ten intervals, with the midpoint of each interval chosen, namely 0.05, 0.15, 0.25, ..., 0.95. Each midpoint is multiplied by the corresponding damage volume, and the sum of all these products is called the “weighted damage volume”.

Differential pressure is defined as the difference between the injection pressure and the production pressure:

$$\Delta p = p_{in,ave} - p_{out,ave} \quad (25)$$

where  $p_{in,ave}$  and  $p_{out,ave}$  are the average pressure of the injection well and production wells, respectively.

$T_{out,ave}$  (°C) is the average temperature of production wells (Song et al., 2018):

$$T_{out,ave}(t) = \frac{1}{L} \int_L T_{out}(t) dl \quad (26)$$

where  $L$  (m) is the length of the production well;  $T_{out}$  (°C) and  $T_{out,ave}$  (°C)

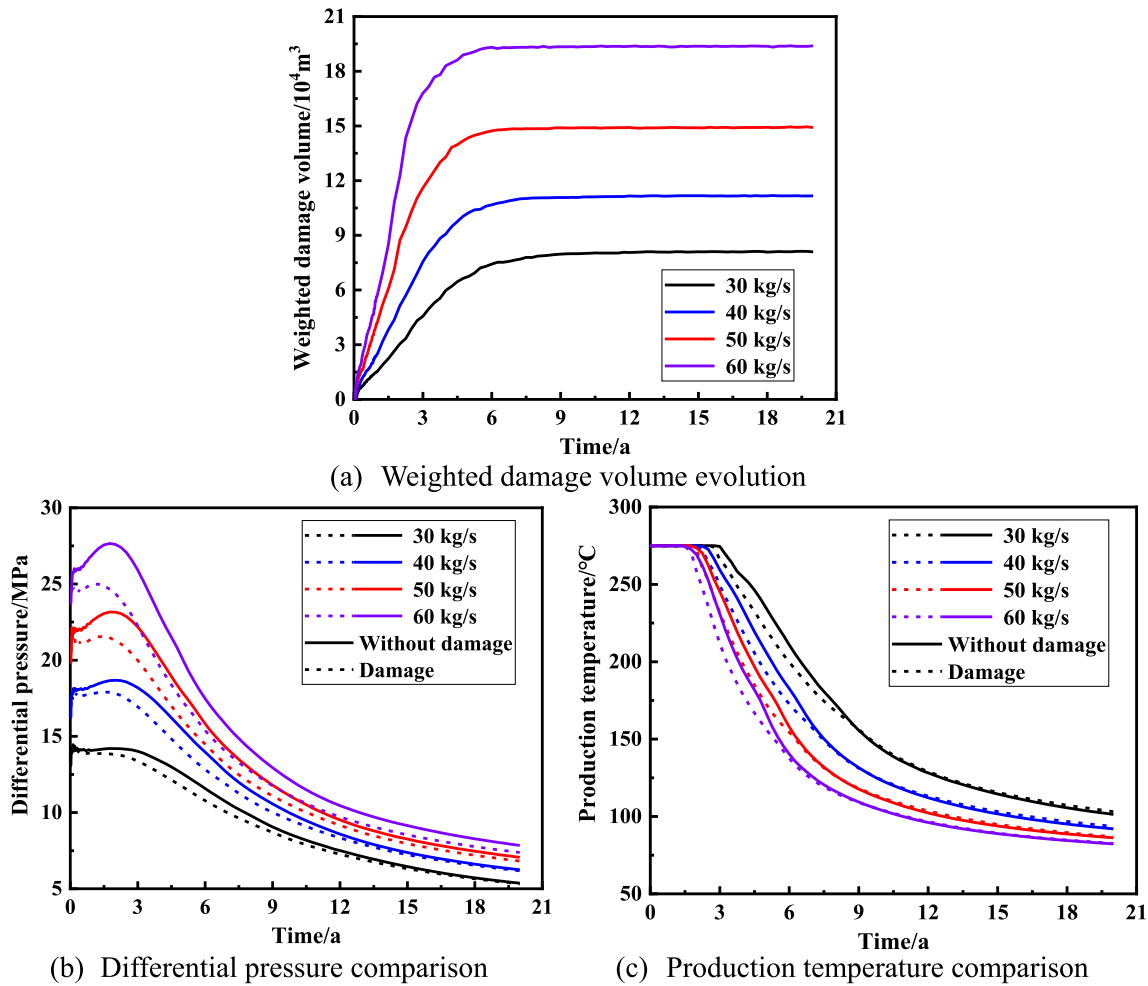


Fig. 12. Characteristics evolution with/without damage at different injection mass flow.

indicate the outlet temperature and average outlet temperature at the well bottom.

Parameters include injection-mining parameters and reservoir physical properties. One control case and eighteen variable cases are set up, and all cases are considered damage or no damage, for a total of thirty-eight cases, as shown in Table 3. The range of values for research parameters is established based on relevant data from the Qiabuqia geothermal field in China (Lei et al., 2020). All parameters for the control case are given in bold form, and other calculation cases are based on the control case to replace the studied variables.

### 3.2. Analysis of evolution characteristics

#### 3.2.1. Multiphysics evolution

The evolutions of temperature, pressure, and stress fields are essential characteristics in production, as shown in Figs. 7 and 8.

From Fig. 7(a), the scope of the low-temperature area gradually increases as production progresses. Regarding vertical temperature distribution, the low-temperature area extends rapidly at the bottom and top of the open reservoir. It is caused by the low production pressure (top) and gravity (bottom), i.e., the above locations where fluids are more likely to aggregate and produce. The central horizontal section of the reservoir is selected for observation, the low-temperature zone extended along the fracture to the substrate on both sides and along the injection well to the production wells. The “fingering phenomenon” is evident, and the low-temperature zone presents a “spindle-shaped” overall, as shown in Fig. 7(b).

From Fig. 7(c), the apparent high-pressure and low-temperature areas appear near the injection well and production wells, respectively, driving the fluid to flow. Due to pressure gradient and gravity in the vertical direction, the “pressure drop funnel” appears near the production wells. On the central horizontal section, the shape of the high-pressure area is similar to the low-temperature area, while the low-pressure area is distributed around the production wells. Moreover, the differential pressure between the injection well and production well decreases with the development, which is caused by increased reservoir permeability due to the matrix elastic deformation and damage.

As mentioned earlier, the maximum tensile stress criterion and More-Coulomb criterion are used to determine damage, as shown in Eq. (18). Correspondingly, the magnitude of  $sp_1$  and  $sp_1 \sim sp_3$  are analyzed, as expressed in Eq. (27).

$$\begin{cases} sp_1 = \sigma_1 \\ sp_1 \sim sp_3 = -\sigma_3 + \sigma_1 \frac{1 + \sin \varphi_f}{1 - \sin \varphi_f} \end{cases} \quad (27)$$

As shown in Fig. 8, there is a similarity in the distribution of  $sp_1 \sim sp_3$  and  $sp_1$ , consistent with the evolution of temperature and pressure fields. It indicates that temperature and pressure changes cause an evolution in the effective stress, especially the thermal stress caused by a temperature drop. However, the corresponding values of  $sp_1$  and  $sp_1 \sim sp_3$  are different. With the center horizontal section as the object, the range of  $sp_1 \sim sp_3$  is  $-140 \text{ MPa} \sim 110 \text{ MPa}$ , while the range of  $sp_1$  is  $-70 \text{ MPa} \sim 30 \text{ MPa}$ . Although the former spans a large range, damage occurs only when  $sp_1 \sim sp_3$  is greater than  $f_c$  or  $sp_1$  is greater than  $f_t$ . The compressive

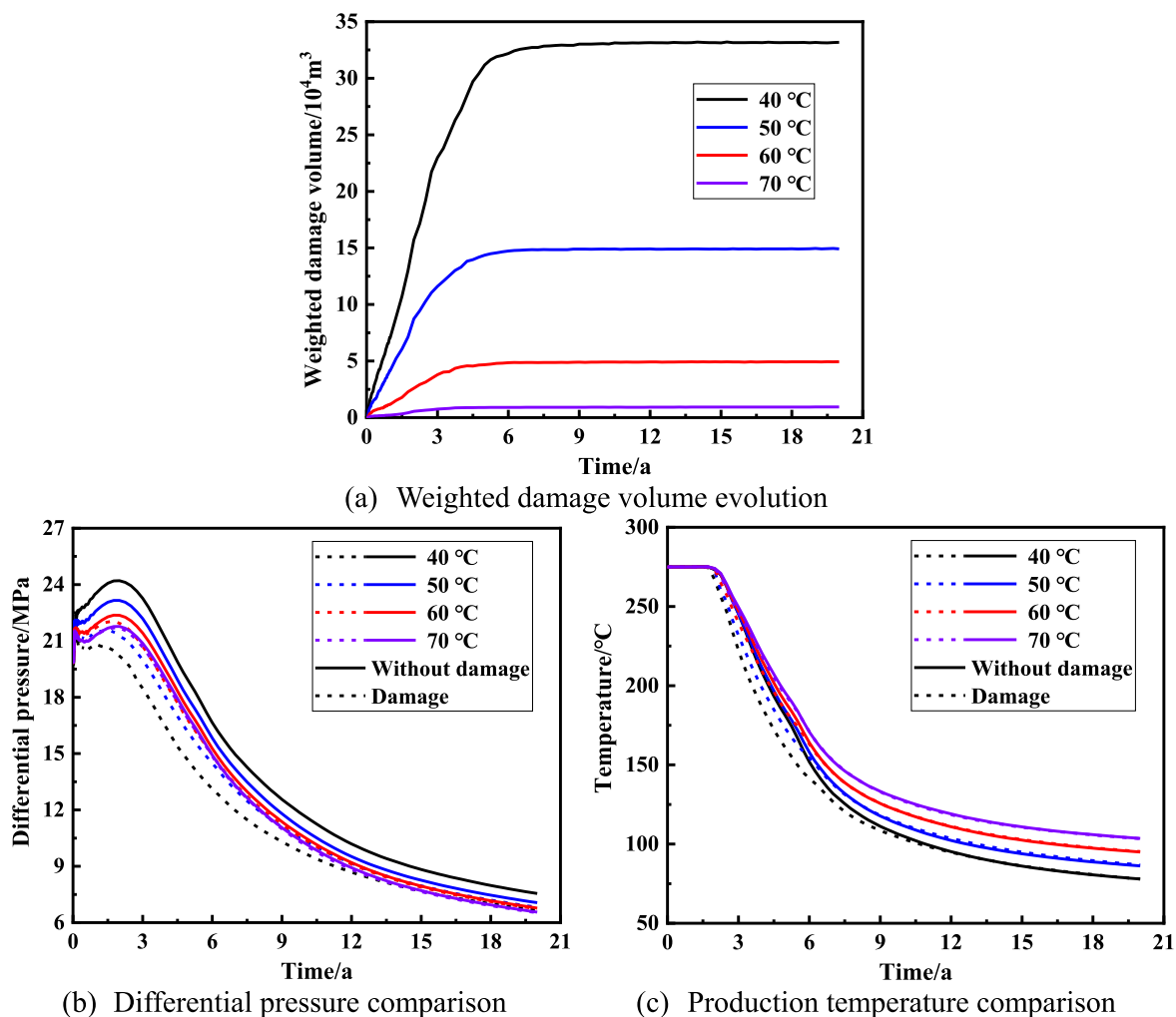


Fig. 13. Characteristics evolution with/without damage at different injection temperatures.

strength (350 MPa) of the rock is much greater than the tensile strength (10.5 MPa). So, the rock is mainly tensile failure during the production process (Xu et al., 2023a), and it is significantly different from the hydraulic fracturing process, which has more significant stress disturbance and easily causes shear failure.

Fig. 9 shows the damage evolution process, similar to the operation of  $sp_1$ ; the damaged area gradually expands from the injection well to the production well. The damaged area is mainly concentrated near the fracture because the temperature drop is most palpable, and the stress disturbance is most severe. In the control case, the maximum damage value is above 0.5, but most damage is between 0 and 0.15, indicating that the damage in the mining process is not dramatic. Moreover, the change in the damaged area is no longer evident after five years. Combined with Fig. 7(b), the temperature “cold front” has reached production well at five years. The evolution of matrix damage near the fracture has ended, while the matrix damage far away from the fracture is more difficult to appear, so the damaged area in the later mining stage is unchanged. Correspondingly, the damage volume gradually increases with time, up to 2.6 million  $m^3$ . The average damage thickness of the damage area can reach up to 6 m and then gradually flattens out, as shown in Fig. 9(c).

### 3.2.2. Damaging effect

According to Eq. (20)-(22), the damage significantly impacts the reservoir’s physical properties. Fig. 10 shows the average damage degree and the average physical properties change at the fracture surface.

As production progresses, the damage degree increases, the corresponding Young’s modulus gradually decreases, and the porosity and permeability increase, consistent with previous experiments’ results (Villarraga et al., 2018; Kang et al., 2021). Among them, the permeability changed the most, from  $3.50 \times 10^{-16}$  at the beginning to  $1.87 \times 10^{-13}$  after stabilization, an increase of more than 500 times. The above phenomenon occurs because of the micro-cracks in the rock matrix caused by damage, which changes internal stress distribution and pore-permeability characteristics. Moreover, the curve changes tend to be stable in the later stage, and the time is almost the same as the previous moment when the temperature “cold front” reaches production well.

Fig. 11 shows differential pressure and temperature with and without damage, which are the key indicators in production. After five years of production at the center section, the maximum pressures are 57.4 MPa and 55.7 MPa, respectively, and the damage reduced the differential pressure by 1.6 MPa. The temperature range is the same in the center section. Still, close to the production well, there is a significant thermal breakthrough (yellow circle area) in the case of considering the damage, as shown in Fig. 11(b), which can lead to lower production temperatures due to thermal breakout in advance.

Differential pressure and production temperature evolution curves also confirm the above rules, as shown in Fig. 11(c) and (d). In the beginning, the slight increase in differential pressure is caused by the increase in fluid viscosity due to temperature drop; the continued decline in the later period is due to the increase in reservoir permeability

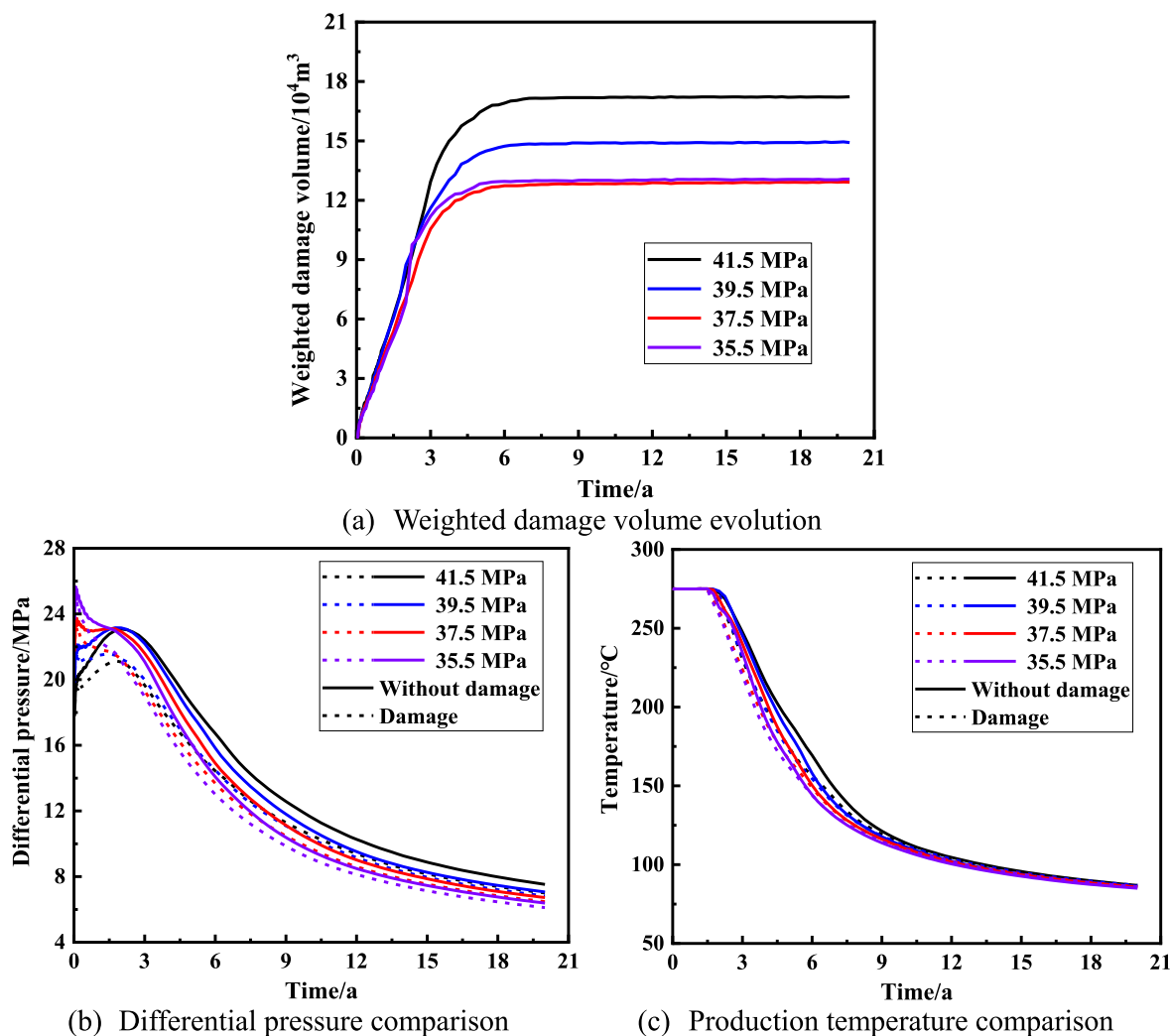


Fig. 14. Characteristics evolution with/without damage at different production pressure.

caused by the elastic deformation/damage of the matrix. The pressure difference without damage is always higher than that of considering the damage, and the maximum difference occurs at 3.25 years, reaching 2.21 MPa, as shown in Fig. 11(c). The above difference rises first and then falls; the initial stage increases because the damage plays a dominant role, the later decline is due to the damage no longer increasing, and the matrix shrinkage caused by elastic deformation significantly increases the fracture aperture to become the dominant factor.

The production temperature evolution curve tends to level at the beginning and gradually decreases, indicating that a thermal breakthrough has occurred at the turning point. Similarly, the temperature is higher without considering damage, and the maximum difference also occurs at 3.25 a, reaching 14.21 °C, as shown in Fig. 11(d). The reason for the above phenomenon is that the damage increases the conductivity near the fracture, which enhances the role of the fracture as the main seepage channel and makes it easier for thermal interference to occur along the fracture. In the later stages of production, damage evolution becomes less prominent (reduced temperature gradient). At this point, matrix elastic deformation takes on a dominant role, and the effect of damage diminishes gradually. There is a reduced difference between considering and not considering damage in terms of temperature variations. The above analysis results indicate that damage research should not be overlooked during heat extraction in high-temperature and high-pressure rock formations.

### 3.3. Influences of key factors

#### 3.3.1. Injection-mining parameter

Injection mass flow is a key design parameter in the mining scheme. Its effect on the production characteristics is shown in Fig. 12. Damage volume at high flow is more significant, and when the mass flow is increased from 30 kg/s to 60 kg/s, the weighted damage volume after stabilization increases from  $8.09 \times 10^4 \text{ m}^3$  to  $19.39 \times 10^4 \text{ m}^3$ , as shown in Fig. 12(a). The temperature drop is more evident because there is more heat transfer between the cold fluid and the matrix at high flow, and the thermal damage degree is more significant.

Affected by the damage, the pressure difference and production temperature decrease in various degrees, and the larger the weighted damage volume, the larger the corresponding change value, as shown in Fig. 12(b)–(c). When the mass flow is from small to large, the maximum value of differential pressure-temperature change is 0.87 MPa–14.35 °C, 1.41 MPa–14.54 °C, 2.21 MPa–14.21 °C, 3.66 MPa–19.10 °C, respectively. By analyzing the ratio of differential pressure change value to the differential pressure without considering the damage, the maximum proportions are 6.96% (30 kg/s), 8.65% (40 kg/s), 10.42% (50 kg/s) and 14.58% (60 kg/s), respectively, and the influence of damage on the change of differential pressure is significant. More, the moment of the above maximum change gradually advanced with the increase of mass flow, which is 4.75 a (30 kg/s), 4.0 a (40 kg/s), 3.25 a (50 kg/s), and 3.0 a (60 kg/s), respectively. Affected by the different flow resistance and

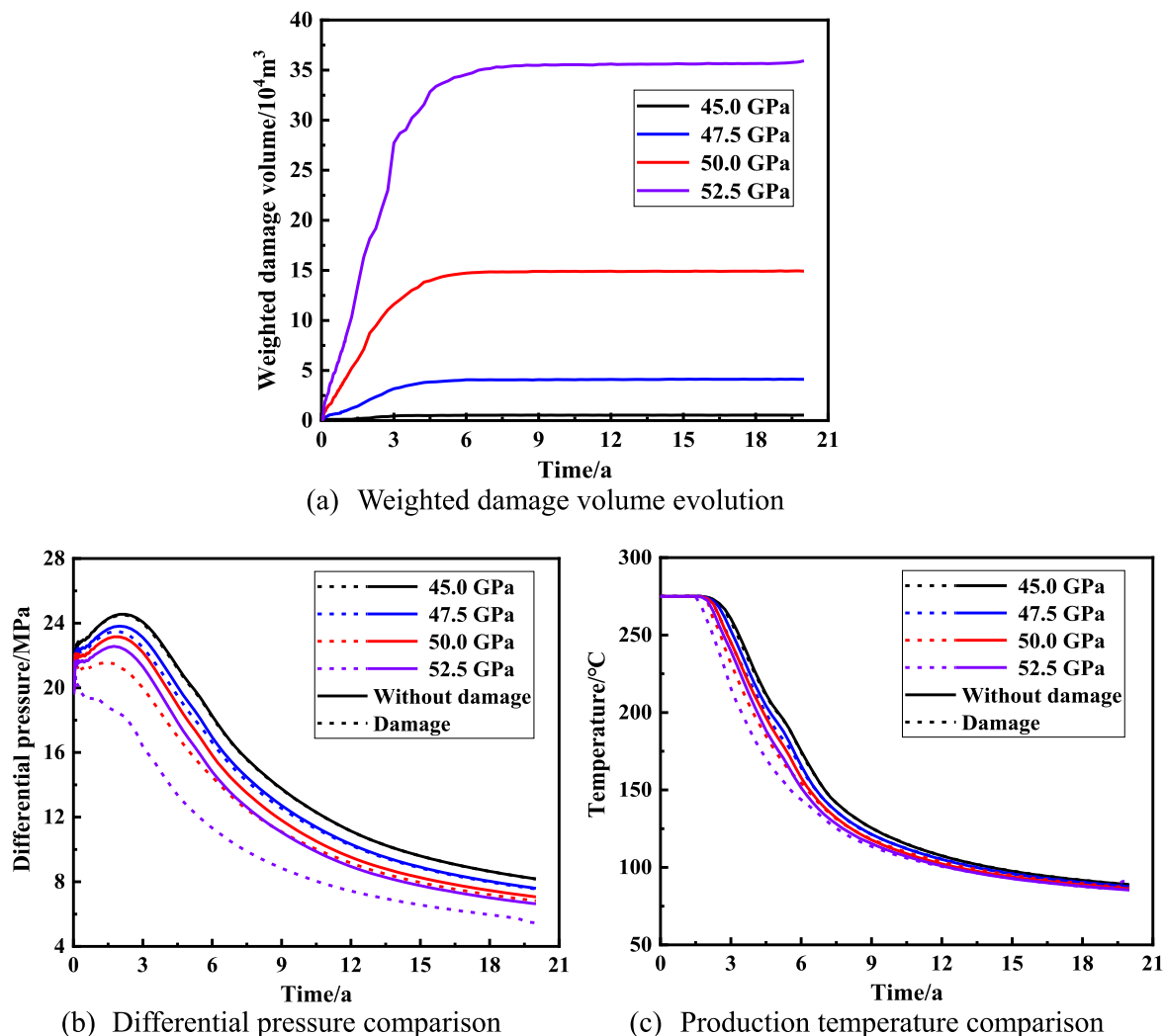


Fig. 15. Characteristics of evolution with/without damage at different Young's modulus.

heat exchange, the differential pressure under high flow is always significant, and the corresponding production temperature is always low, which has been widely proven in previous studies (Xu et al., 2023b).

The treated water is recharged into geothermal reservoirs to reduce water waste and environmental pollution. Recharge temperature varies depending on the cascade utilization, and Fig. 13 shows the production characteristics at different temperatures. At low injection temperatures, it is more likely to cause significant damage, which is related to the magnitude of induced thermal stress. When the injection temperature is increased from 40 °C to 70 °C, the weighted damage volume after stabilization decreases from  $33.18 \times 10^4 \text{ m}^3$  to  $0.94 \times 10^4 \text{ m}^3$ , as shown in Fig. 13(a).

In terms of the influence effect of differential pressure change, the effect of temperature is higher than that of mass flow under the study conditions in this paper. When the injection temperature is from 40 °C to 70 °C, the maximum value of differential pressure-temperature change is 4.82 MPa–24.30 °C, 2.21 MPa–14.21 °C, 0.74 MPa–7.42 °C, 0.22 MPa–3.34 °C, respectively. The maximum proportions for the ratio of differential pressure change value to the differential pressure without considering damage are 22.69% (40 °C), 10.42% (50 °C), 3.65% (60 °C), and 1.07% (70 °C), respectively. Moreover, from Fig. 13(b), the curves corresponding to 40 °C with or without damage are located at the bottom and top of all curves, respectively, the former because of the large flow resistance caused by the high viscosity of the fluid at low temperatures, and the latter because the damage at low temperatures

significantly increases the reservoir permeability.

Fig. 14 shows a comparison of production characteristics at different average production pressures. With the increase in production pressure, the damage volume shows an upward trend caused by the disturbance of the stress field. Regardless of damage, high production pressures correspond to higher injection-mining pressure differences and production temperatures. For example, after ten years of production, the above production characteristic values at a production pressure of 41.5 MPa are 2.07 MPa and 5.42 °C higher than 35.5 MPa. It indicates that at higher production pressures, the flow resistance of the fluid in the reservoir becomes greater. Affected by damage, when the average production pressure is from 41.5 MPa to 35.5 MPa, the maximum value of differential pressure-temperature change is 2.95 MPa–18.44 °C, 2.21 MPa–14.21 °C, 2.33 MPa–16.49 °C, 2.13 MPa–15.61 °C, respectively. Overall, the change is on a downward trend.

### 3.3.2. Reservoir physical parameters

Young's modulus and Poisson's ratio are important mechanical properties of rocks. Young's modulus is the elastic modulus along the longitudinal direction, and Poisson's ratio is the elastic constant reflecting the lateral deformation. Figs. 15 and 16 show the production characteristics under the above mechanical property, respectively.

The weighted damage volume gradually increased with the increase of Young's modulus and Poisson's ratio. For example, when the average Young's modulus increases from 45.0 GPa to 52.5 GPa, the weighted

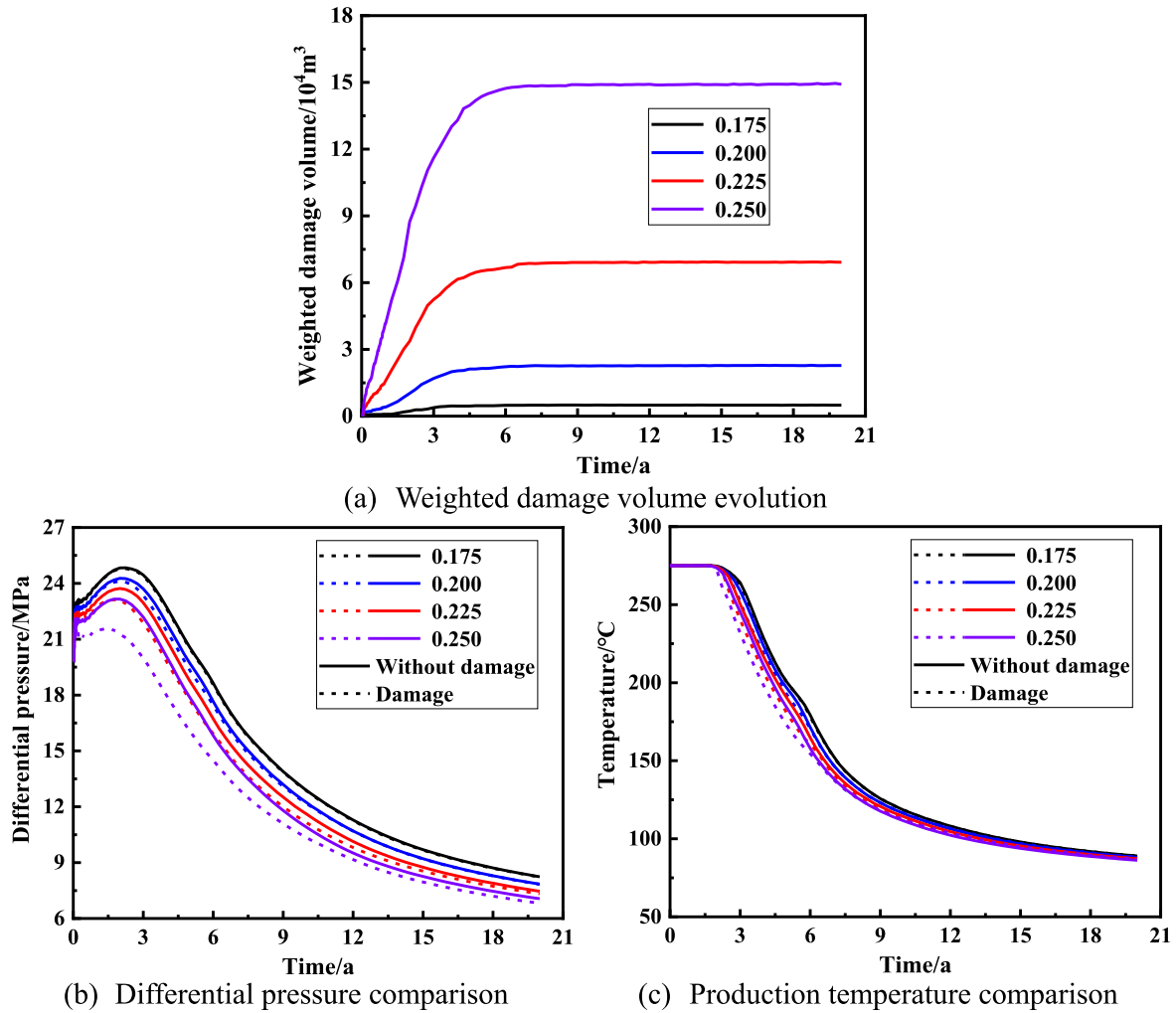


Fig. 16. Characteristics evolution with/without damage at different Poisson's ratio.

damage volume after stabilization increases from  $0.54 \times 10^4 \text{ m}^3$  to  $35.93 \times 10^4 \text{ m}^3$ , as shown in Fig. 15(a). When the average Poisson's ratio increases from 0.175 to 0.250, the weighted damage volume after stabilization increases from  $0.49 \times 10^4 \text{ m}^3$  to  $14.91 \times 10^4 \text{ m}^3$ , as shown in Fig. 16(a). From Eq. (16), the volumetric elastic modulus of the porous medium in the thermal stress term is directly proportional to Young's modulus ( $E$ ) of the rock and inversely proportional to Poisson's ratio expression (1-2  $\nu$ ). Thus, the increase in Young's modulus and Poisson's ratio results in more significant thermal stress at the same temperature gradient, i.e., damage evolution is more pronounced.

Affected by damage, when the average Young's modulus is from 45.0 MPa to 52.5 MPa, the maximum value of differential pressure-temperature change is 0.13 MPa–2.61 °C, 0.67 MPa–7.80 °C, 2.21 MPa–14.21 °C, 4.95 MPa–24.56 °C, respectively. Moreover, when the average Poisson's ratio is from 0.175 to 0.250, the maximum value of differential pressure-temperature change is 0.09 MPa–2.04 °C, 0.43 MPa–8.34 °C, 1.16 MPa–10.48 °C, 2.21 MPa–14.21 °C, respectively. Although the above characteristics changes showed an upward trend, with the uniform increase of mechanical property values, the change range of above production characteristics gradually increased, indicating that characteristics evolution is more sensitive under high property values.

Fig. 17 shows the production characteristics under different fracture initial permeability. Within the parameters and research scope of this paper, the fracture's initial permeability has little influence on damage evolution. The weighted damage volume gradually decreases with the

fracture's initial permeability increase. Correspondingly, when the average initial permeability is from  $2.0 \times 10^{-11} \text{ m}^2$  to  $6.5 \times 10^{-11} \text{ m}^2$ , the maximum value of differential pressure-temperature change is 2.58 MPa–15.86 °C, 2.21 MPa–14.21 °C, 2.31 MPa–18.45 °C, 1.96 MPa–14.95 °C, respectively. There is no obvious pattern in the above phenomenon. However, in terms of no damage, the larger fracture initial permeability will reduce the injection pressure, reducing the difficulty of mining geothermal reservoirs, but the production temperature drops faster. Therefore, in actual production, an excessive increase in fracture permeability will accelerate the thermal breakthrough of the system, reduce its operating life, and is not conducive to heat extraction.

#### 4. Economic characteristics discussion

##### 4.1. Economic evaluation indicators

From the above analysis, for the identified reservoirs, well types, and production modes, the damage significantly impacts differential pressure and production temperature, impacting operating expenses and earnings. To analyze the effect of damage on the economic benefits for EGS projects, the differential economic benefits are defined (Kong et al., 2017; Cui et al., 2023):

$$\begin{cases} \Delta C = -\Delta C_{pump} + \Delta C_T - \Delta C_o \\ \Delta C_{pump} = p_e (q_{ave,y,d} P_d - q_{ave,y,nd} P_{nd}) / \eta_p \\ \Delta C_T = p_T \eta_T (q_{ave,y,d} \rho_{f,d} c_{p,f,d} T_d - q_{ave,y,nd} \rho_{f,nd} c_{p,f,nd} T_{nd}) \\ \Delta C_o = \Delta C_w + \Delta C_m + \Delta C_l \end{cases} \quad (28)$$

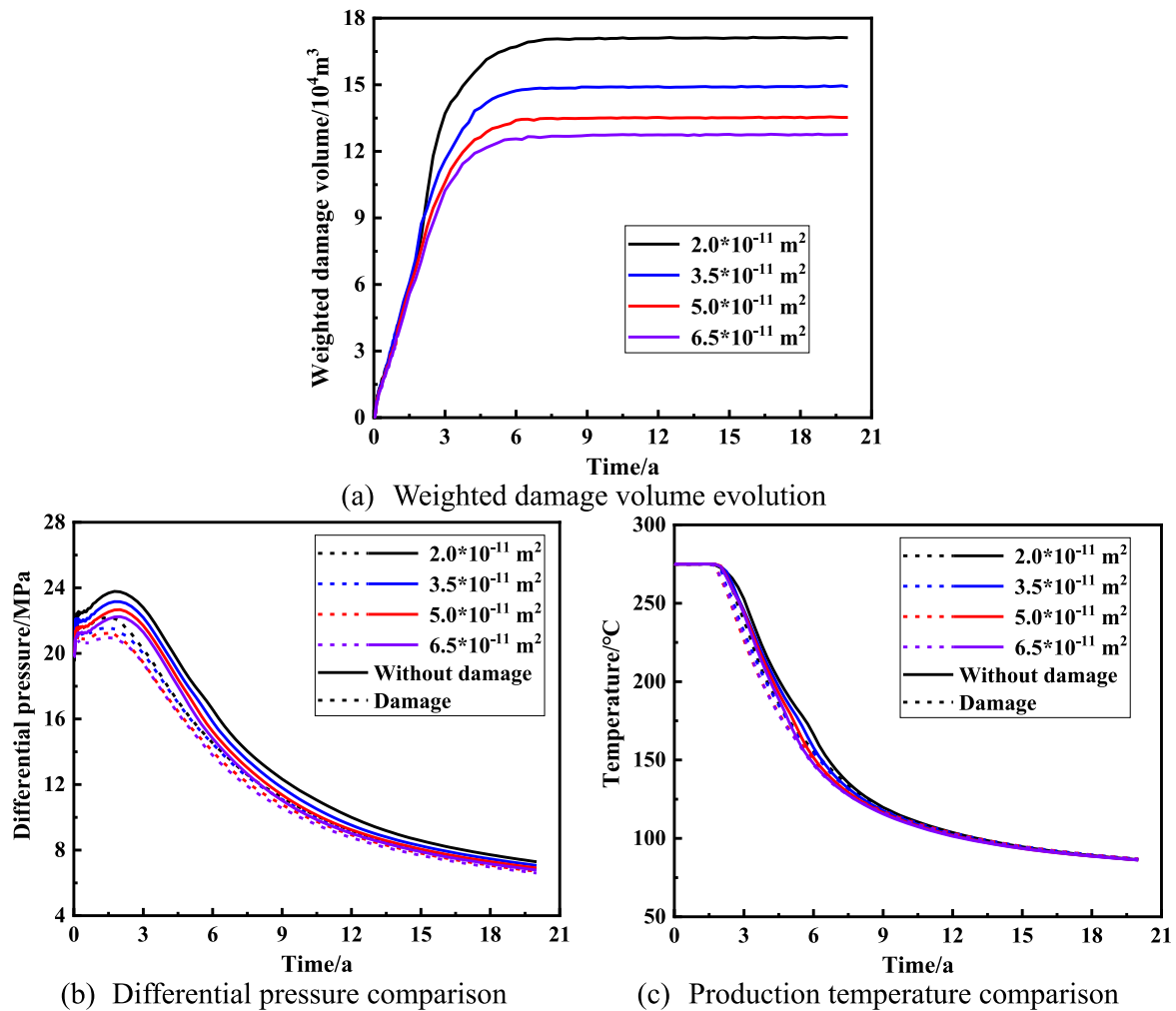


Fig. 17. Characteristics evolution with/without damage at different fracture initial permeability.

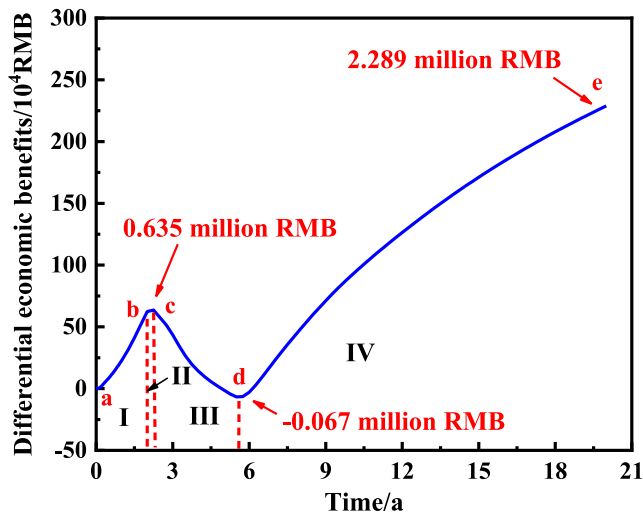


Fig. 18. Differential economic benefit.

where  $C_{pump}$  (RMB) is the additional cost of electricity due to varying pressure differences;  $C_T$  (RMB) is the benefits from heat extraction changes;  $C_o$  (RMB) is the other cost incurred due to tailwater treatment

( $C_w$ ), post-maintenance ( $C_m$ ) and labor services ( $C_l$ );  $p_e$  (0.45 RMB/kW.h) and  $p_T$  (0.22 RMB/kW.h) are the prices of electrical power and heat application, respectively (Xu et al., 2023b);  $q_{ave,v,d}$  and  $q_{ave,v,nd}$  ( $m^3/s$ ) are the volume flow considering the damage and not;  $p_d$  (Pa) and  $p_{nd}$  (Pa) are the injection-mining pressure difference considering damage and not, respectively;  $\eta_p$  (75.0%) is the pump efficiency, representing the conversion efficiency between electrical and mechanical energy (Wang et al., 2020b);  $\eta_T$  (12.0%) is the efficiency of geothermal power generation (Zarrouk and Moon, 2014);  $T_d$  ( $^{\circ}C$ ) and  $T_{nd}$  ( $^{\circ}C$ ) are the temperature difference considering damage and not, respectively.

#### 4.2. Comparison with or without damage

As shown in Fig. 11(c) and (d), the differential pressure and production temperature under the condition of damage are lower than those without damage. Fig. 18 shows the evolution curve of differential economic benefit ( $\Delta C$ ), and the curve can be roughly divided into four stages:

- Stage I (a-b): The curve rises sharply in a short period, and no thermal breakthrough has occurred at this stage, so there is no significant change in the production temperature in both cases. The appearance of damage reduces the differential pressure; the electricity required to operate the pump is reduced.
- Stage II (b-c): Thermal breakthrough at point b has already occurred, and the lower production temperature under the condition of

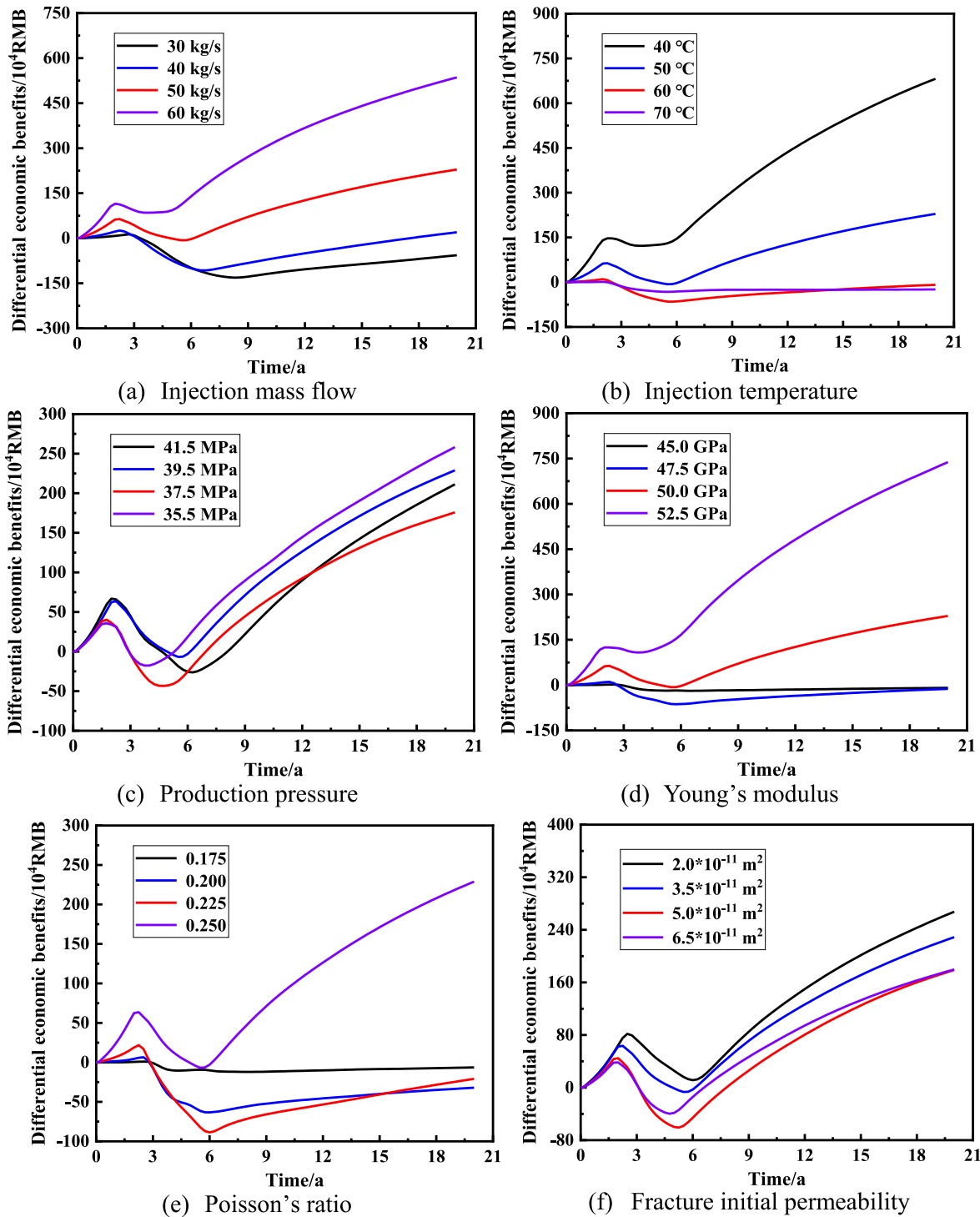


Fig. 19. Comparison of differential economic benefit with/without damage under multiple parameters.

damage has affected its economic gains. However, the reduced electricity spending due to the reduction of differential pressure is still dominant, so the curve at this stage is upward, and the increase gradually decreases. A local maximum is observed, which is 635,000 RMB.

Stage III (c-d): In this stage, the difference between the differential pressure gradually decreases and the production temperature dominates. During this stage, the minimum value occurs at point d, which is -67,000 RMB. Production temperature under the condition of

damage is low, as shown in Fig. 11(d), which leads to poor economic benefits, so the curve shows a downward trend.

Stage IV (d-e): In the later mining stage, the production temperature in both cases is almost the same. The differential pressure value in the case of damage is always less than that of the case without damage, so the economic benefit of the former is always higher than that of the latter. As the differential pressure between the two cases decreases, the slope of the d-e segment gradually decreases. In 20 a, the difference in cumulative economic benefits reached the maximum, at 2.289 million RMB, as shown in Fig. 18.

The above results show that under the model and parameter settings in this paper, the economic benefits of HDR mining considering damage are higher for the case when damage is not considered. However, the value size of differential economic benefits and even positive and negative values are also related to the price and parameter range, and the specific benefits should be judged according to the actual situation.

#### 4.3. Influences of various parameters

Fig. 19 compares differential economic benefits with/without damage under multiple parameters. It can be concluded that each curve has an upward-down-upward trend, similar to the curve in Fig. 18. The effects of injection temperature, Young's modulus, and injection mass flow on the differential economic benefits are significant, followed by Poisson's ratio. In contrast, production pressure and fracture initial permeability had less influence.

Take the effect of injection mass flow as an example. When its values are from 30 kg/s to 60 kg/s, the differential economic benefits are  $-56.69 \times 10^4$  RMB,  $19.86 \times 10^4$  RMB,  $228.90 \times 10^4$  RMB,  $535.85 \times 10^4$  RMB at 20 a, respectively. In addition to the negative economic benefit at low injection mass flow, negative values will occur at high injection temperature, low Young's modulus, and Poisson's ratio. Because the damage degree is small now, reducing pressure difference's economic benefit is less than lowering production temperature. The above damage analysis can help the geothermal development scheme design to be more realistic and have higher economic returns.

## 5. Conclusion

To analyze the effect of damage on the long-term heat extraction process of hot dry rocks, it established a three-dimensional field-scale THM-D model, analyzed damage evolution characteristics and production performances, and compared the economic benefits of geothermal systems considering damage or not. The main conclusions of this paper are as follows:

- (1) Damage is mainly affected by thermal stress, and damage changes no longer significantly after the thermal breakthrough. Damage evolution is from the injection well to the production well, and from fracture to matrix on both sides. By analyzing the relationship between effective principal stress and tensile/compressive strength, rock is mainly tensile failure during the production process.
- (2) As production progresses, the damage degree increases, the corresponding Young's modulus gradually decreases, and the porosity and permeability increase. Permeability changed the most, with a more than 500 times increase after damage. Damage will cause the differential pressure and production temperature to drop, and the maximum reduction of the control case can reach 2.21 MPa and 14.21 °C.
- (3) Weighted damage volume increased significantly with high injection mass flow, low injection temperature, high production pressure, high Young's modulus and Poisson's ratio, and low fracture initial aperture. The larger the weighted damage volume, the greater the corresponding differential pressure and production temperature drop.
- (4) The differential economic benefits change curve is roughly divided into four stages: sharp rise-slow rise-decline-slow rise; the key lies in the dominant role of differential pressure change or production temperature change. The effects of injection temperature, Young's modulus, and injection mass flow on the differential economic benefits are significant, followed by Poisson's ratio. At the same time, production pressure and fracture initial permeability had less influence. The maximum differential economic benefit is up to 2.289 million RMB.

- (5) The current study focuses on a single fractured reservoir. Future analyses will extend to complex fractured reservoirs, considering the impact of water-rock interactions on damage evolution.

## CRedit authorship contribution statement

**Fuqiang Xu:** Formal analysis, Investigation, Methodology, Writing – original draft. **Yu Shi:** Conceptualization, Software, Supervision, Project administration. **Xianzhi Song:** Data curation, Funding acquisition, Resources. **Guofeng Song:** Conceptualization, Writing-review. **Shuang Li:** Writing-review.

## Declaration of competing interest

The authors declare that they have no known competing financial interests or personal relationships that could have appeared to influence the work reported in this paper.

## Data availability

Data will be made available on request.

## Acknowledgments

The authors would like to acknowledge the National Natural Science Foundation of China (Grant No. 52104034), the Major Program of the National Natural Science Foundation of China (Grant No. 52192624), the New Interdisciplinary Discipline Cultivation Fund of Southwest Jiaotong University (Grant No. 2682023ZTPY030, 2682022KJ034), the China Scholarship Council (Grant No. 202206440098). Moreover, thanks to Ms. Han Xiao.

## References

- Biot, M.A., 1962. Mechanics of deformation and acoustic propagation in porous media. *J. Appl. Phys.* 33 (4), 1482–1498.
- Chen, Y., Ma, G., Wang, H., Li, T., Wang, Y., 2019. Application of carbon dioxide as working fluid in geothermal development considering a complex fractured system. *Energy Convers. Manag.* 180, 1055–1067.
- Cheng, L., Luo, Z., Xie, Y., Zhao, L., Wu, L., 2023. Numerical simulation and analysis of damage evolution and fracture activation in enhanced tight oil recovery using a THMD coupled model. *Comput. Geotech.* 155, 105244.
- Cui, Q., Shi, Y., Zhang, Y., Wu, R., Jiao, Y., 2023. Comparative study on the thermal performance and economic efficiency of vertical and horizontal ground heat exchangers. *Adv. Geo-Energy Res.* 7 (1), 7–19.
- Guo, T., Tang, S., Liu, S., Liu, X., Zhang, W., Qu, G., 2020. Numerical simulation of hydraulic fracturing of hot dry rock under thermal stress. *Eng. Fract. Mech.* 240, 107350.
- Guo, T., Zhang, Y., Zhang, W., Niu, B., He, J., Chen, M., Yu, Y., Xiao, B., Xu, R., 2022. Numerical simulation of geothermal energy productivity considering the evolution of permeability in various fractures. *Appl. Therm. Eng.* 201, 117756.
- Hofmann, H., Blöcher, G., Milsch, H., Babadagli, T., Zimmermann, G., 2016. Transmissivity of aligned and displaced tensile fractures in granitic rocks during cyclic loading. *Int. J. Rock Mech. Min. Sci.* 87, 69–84.
- Holzbecher, E., 1998. *Modeling Density-Driven Flow in Porous Media*. Springer.
- Ijeje, J., Gan, Q., Cai, J., 2019. Influence of permeability anisotropy on heat transfer and permeability evolution in geothermal reservoir. *Adv. Geo-Energy Res.* 3 (1), 43–51.
- Ju, B., Wu, Y., Fan, T., 2011. Study on fluid flow in nonlinear elastic porous media: experimental and modeling approaches. *J. Pet. Sci. Eng.* 76, 205–211.
- Kang, F., Jia, T., Li, Y., Deng, J., Tang, C., Huang, X., 2021. Experimental study on the physical and mechanical variations of hot granite under different cooling treatments. *Renew. Energy* 179, 1316–1328.
- Kong, Y., Pang, Z., Shao, H., Kolditz, O., 2017. Optimization of well-doublet placement in geothermal reservoirs using numerical simulation and economic analysis. *Environ. Earth Sci.* 76 (3), 118.
- Lei, Z., Zhang, Y., Zhang, S., Fu, L., Hu, Z., Yu, Z., Li, L., Zhou, J., 2020. Electricity generation from a three-horizontal-well enhanced geothermal system in the Qiabua geothermal field, China: Slickwater fracturing treatments for different reservoir scenarios. *Renew. Energy* 145, 65–83.
- Lei, Q., Doonechaly, N., Tsang, C., 2021. Modelling fluid injection-induced fracture activation, damage growth, seismicity occurrence and connectivity change in naturally fractured rocks. *Int. J. Rock Mech. Min. Sci.* 138, 104598.
- Li, Z., Li, L., Huang, B., Zhang, L., Li, M., Zuo, J., Li, A., Yu, Q., 2017. Numerical investigation on the propagation behavior of hydraulic fractures in shale reservoir based on the DIP technique. *J. Pet. Sci. Eng.* 154, 302–314.

- Li, X., 2018. Research on Flow-Heat Transfer and Rock Damage during CO<sub>2</sub> Fracturing Based on Multiphysics Coupling. China University of Petroleum (Beijing), China.
- Li, N., Zhang, S., Ma, X., Zou, Y., Li, S., Zhang, Z., 2020. Thermal effect on the evolution of hydraulic fracture conductivity: an experimental study of enhanced geothermal system. *J. Pet. Sci. Eng.* 187, 106814.
- Liu, L., Ji, H., Elsworth, D., Zhi, S., Lv, X., Wang, T., 2020. Dual-damage constitutive model to define thermal damage in rock. *Int. J. Rock Mech. Min. Sci.* 126, 104185.
- Rutqvist, J., Børgesson, L., Chijimatsu, M., Kobayashi, A., Jing, L., Nguyen, T., Noorishad, J., Tsang, C., 2001. Thermohydraulics of partially saturated geological media: governing equations and formulation of four finite element models. *Int. J. Rock Mech. Min. Sci.* 38, 105–127.
- Shi, Y., Song, X., Li, J., Wang, G., Zheng, R., YuLong, F., 2019a. Numerical investigation on heat extraction performance of a multilateral-well enhanced geothermal system with a discrete fracture network. *Fuel* 244, 207–226.
- Shi, Y., Song, X., Wang, G., Li, J., Geng, L., Li, X., 2019b. Numerical study on heat extraction performance of the enhanced geothermal systems considering complex hydraulic and natural fractures. *Renew. Energy* 141, 950–963.
- Shi, Y., Xu, F., Song, X., Wang, G., Zuo, Y., Li, X., Ji, J., 2023. Rock damage evolution in the production process of the enhanced geothermal systems considering thermal-hydrological-mechanical and damage (THM-D). *Energy* 285, 129421.
- Shu, B., Zhu, R., Elsworth, D., Dick, J., Liu, S., Tan, J., Zhang, S., 2020. Effect of temperature and confining pressure on the evolution of hydraulic and heat transfer properties of geothermal fracture in granite. *Appl. Energy* 272, 115290.
- Song, X., Shi, Y., Li, G., Yang, R., Wang, G., Zheng, R., Li, J., Lyu, Z., 2018. Numerical simulation of heat extraction performance in enhanced geothermal system with multilateral wells. *Appl. Energy* 218, 325–337.
- Song, G., Shi, Y., Xu, F., Song, X., Li, G., Wang, G., Lv, Z., 2024. The magnitudes of multi-physics effects on geothermal reservoir characteristics during the production of enhanced geothermal system. *J. Clean. Prod.* 434, 140070.
- Song, G., Song, X., Xu, F., Li, G., Shi, Y., Ji, J., 2022. Contributions of thermo-poroelastic and chemical effects to the production of enhanced geothermal system based on thermo-hydro-mechanical-chemical modeling. *J. Clean. Prod.* 377, 134471.
- Sun, Z., Jiang, C., Wang, X., Lei, Q., Jourde, H., 2020. Joint influence of in-situ stress and fracture network geometry on heat transfer in fractured geothermal reservoirs. *Int. J. Heat Mass Tran.* 149, 119216.
- Taler, D., 2019. Numerical Modelling and Experimental Testing of Heat Exchangers. Springer International Publishing, Cham, Switzerland.
- Tarkowski, R., Uliasz-Misiak, B., 2019. Prospects for the use of carbon dioxide in enhanced geothermal systems in Poland. *J. Clean. Prod.* 229, 1189–1197.
- Villarraga, C., Gasc-Barbier, M., Vaunat, J., Darozes, J., 2018. The effect of thermal cycles on limestone mechanical degradation. *Int. J. Rock Mech. Min. Sci.* 109, 115–123.
- Wang, G., Song, X., Shi, Y., Zheng, R., Li, J., Li, Z., 2020a. Production performance of a novel open loop geothermal system in a horizontal well. *Energy Convers. Manag.* 206, 112478.
- Wang, G., Song, X., Shi, Y., Yulong, F., Yang, R., Li, J., 2020b. Comparison of production characteristics of various coaxial closed-loop geothermal systems. *Energy Convers. Manag.* 225, 113437.
- Wang, G., Ma, X., Song, X., Li, G., 2022. Modeling flow and heat transfer of fractured reservoir: implications for a multi-fracture enhanced geothermal system. *J. Clean. Prod.* 365, 132708.
- Wang, D., Dong, Y., Wang, Q., Sun, D., Yu, B., 2023. Experimental study on the evolution of mechanical properties of hot dry rocks under alternating temperature loads. *Geothermics* 107, 102599.
- Wei, C., Zhu, W., Yu, Q., Xu, T., Jeon, S., 2015. Numerical simulation of excavation damaged zone under coupled thermal-mechanical conditions with varying mechanical parameters. *Int. J. Rock Mech. Min. Sci.* 75, 169–181.
- Witherspoon, P., Amick, C., Gale, J., Iwai, K., 1979. Observations of a potential size effect in experimental determination of the hydraulic properties of fractures. *Water Resour. Res.* 15 (5), 1142–1146.
- Xu, T., Liang, X., Xia, Y., Jiang, Z., Gherardi, F., 2022. Performance evaluation of the Habanero enhanced geothermal system, Australia: optimization based on tracer and induced micro-seismicity data. *Renew. Energy* 181, 1197–1208.
- Xu, F., Ma, T., Tang, Y., Song, X., Shi, Y., 2021. Evaluation of heat extraction performance for vertical multi-fractures in enhanced geothermal system. *Energy Sources, Part A Recovery, Util. Environ. Eff.* 1–22.
- Xu, F., Shi, Y., Song, X., Li, G., Song, Z., Li, S., 2023a. The characteristics and laws of fracture damage in the long-term production process of high-temperature geothermal resources. *Rock Mech. Rock Eng.* 56, 275–299.
- Xu, F., Song, X., Song, G., Ji, J., Song, Z., Shi, Y., Lv, Z., 2023b. Numerical studies on heat extraction evaluation and multi-objective optimization of abandoned oil well patterns in intermittent operation mode. *Energy* 269, 126777.
- Yang, R., Wang, Y., Song, G., Shi, Y., 2023. Fracturing and thermal extraction optimization methods in enhanced geothermal systems. *Adv. Geo-Energy Res.* 9 (2), 136–140.
- Yu, P., Dempsey, D., Archer, R., 2022. Techno-Economic feasibility of enhanced geothermal systems (EGS) with partially bridging Multi-Stage fractures for district heating applications. *Energy Convers. Manag.* 257, 115405.
- Zarrouk, S., Moon, H., 2014. Efficiency of geothermal power plants: a worldwide review. *Geothermics* 51, 142–153.
- Zhang, S., Huang, Z., Wang, H., Zhang, H., Zhang, C., Xiong, C., 2018. Thermal characteristics analysis with local thermal non-equilibrium model during liquid nitrogen jet fracturing for HDR reservoirs. *Appl. Therm. Eng.* 143, 482–492.
- Zhang, X., Huang, Z., Lei, Q., Yao, J., Gong, L., Sun, Z., Yang, W., Yan, X., Li, Y., 2021. Impact of fracture shear dilation on long-term heat extraction in Enhanced Geothermal Systems: insights from a fully-coupled thermo-hydro-mechanical simulation. *Geothermics* 96, 102216.
- Zhang, W., Wang, Z., Guo, T., Wang, C., Li, F., Qu, Z., 2022. The enhanced geothermal system heat mining prediction based on fracture propagation simulation of thermo-hydro-mechanical-damage coupling: insight from the integrated research of heat mining and supercritical CO<sub>2</sub> fracturing. *Appl. Therm. Eng.* 215, 118919.
- Zhang, B., Guo, T., Qu, Z., Wang, J., Chen, M., Liu, X., 2023. Numerical simulation of fracture propagation and production performance in a fractured geothermal reservoir using a 2D FEM-based THMD coupling model. *Energy* 273, 127175.
- Zhong, C., Xu, T., Yuan, Y., Feng, B., Yu, H., 2022. The feasibility of clean power generation from a novel dual-vertical-well enhanced geothermal system (EGS): a case study in the Gonghe Basin, China. *J. Clean. Prod.* 344, 131109.
- Zhong, C., Xu, T., Yuan, Y., Cui, G., Gherardi, F., Li, X., 2023. Coupled effects of elastic and plastic deformation on hydraulic properties of the geothermal fracture induced by cyclic loading-unloading processes. *Eng. Geol.* 313, 106929.
- Zhu, W., Tang, C., 2004. Micromechanical model for simulating the fracture process of rock. *Rock Mech. Rock Eng.* 37 (1), 25–56.
- Zhu, W., Wei, C., 2011. Numerical simulation on mining-induced water inrushes related to geologic structures using a damage-based hydromechanical model. *Environ. Earth Sci.* 62, 43–54.
- Zhu, W., Wei, C., Li, S., Wei, J., Zhang, M., 2013. Numerical modeling on distress blasting in coal seam for enhancing gas drainage. *Int. J. Rock Mech. Min. Sci.* 59, 179–190.
- Zhu, W., Wei, J., Zhao, J., Niu, L., 2014. 2D numerical simulation on excavation damaged zone induced by dynamic stress redistribution. *Tunn. Undergr. Space Technol.* 43, 315–326.
- Zhu, Z., Yang, S., Ranjith, P., Tian, W., Tian, H., Zheng, J., Jiang, G., Dou, B., 2023. A comprehensive review on mechanical responses of granite in enhanced geothermal systems (EGSS). *J. Clean. Prod.* 383, 135378.